New functionalities in abundant element oxides: ubiquitous element strategy

2011 Sci. Technol. Adv. Mater. 12 034303

(http://iopscience.iop.org/1468-6996/12/3/034303)

IOP PUBLISHING SCIENCE AND TECHNOLOGY OF ADVANCED MATERIALS

Sci. Technol. Adv. Mater. **12** (2011) 034303 (22pp) doi:10.1088/1468-6996/12/3/034303

TOPICAL REVIEW

New functionalities in abundant element oxides: ubiquitous element strategy

Hideo Hosono[1,2,3], Katsuro Hayashi[2], Toshio Kamiya[2,3], Toshiyuki Atou[2] and Tomofumi Susaki[2,4]

[1] Frontier Research Center, Tokyo Institute of Technology, 4259 Nagatsuta, Midori, Yokohama 226-8503, Japan
[2] Secure Materials Center, Materials and Structures Laboratory, Tokyo Institute of Technology, Nagatsuta, Midori, Yokohama 226-8503, Japan
[3] Materials and Structures Laboratory, Tokyo Institute of Technology, Nagatsuta, Midori, Yokohama 226-8503, Japan
[4] Japan Science and Technology Agency, Kawaguchi, Saitama 332-0012, Japan

E-mail: susaki@msl.titech.ac.jp

Received 31 January 2011
Accepted for publication 9 May 2011
Published 16 June 2011
Online at stacks.iop.org/STAM/12/034303

Abstract
While most ceramics are composed of ubiquitous elements (the ten most abundant elements within the Earth's crust), many advanced materials are based on rare elements. A 'rare-element crisis' is approaching owing to the imbalance between the limited supply of rare elements and the increasing demand. Therefore, we propose a 'ubiquitous element strategy' for materials research, which aims to apply abundant elements in a variety of innovative applications. Creation of innovative oxide materials and devices based on conventional ceramics is one specific challenge. This review describes the concept of ubiquitous element strategy and gives some highlights of our recent research on the synthesis of electronic, thermionic and structural materials using ubiquitous elements.

Keywords: functional oxides, abundant elements, zirconia, atomic oxygen, oxidation, mass spectroscopy, mullite, aluminosilicate, nanofragmentation, phase transition, shock wave, MgO, thin film growth, polar surface

1. Introduction: ubiquitous element strategy in materials science

Although more than 100 elements are known to exist to date, only 60–70 of them are available for practical materials because of abundance, toxicity and radioactivity issues. The Earth's crust is primarily composed of oxides of main-group elements such as Si, Al, Ca, Na, Mg and so on. Iron and titanium are the only two transition metals within the ten most common elements. The present information era relies on silicon (memory and central processing units in the computer) and silicon dioxide (optical fibers). It is natural to consider that the coming era, which is facing energy, resource management and environmental issues, should be supported by innovative materials based on abundant elements. We call the approach to realize important material functions using abundant elements the *ubiquitous element strategy*. This strategy may be regarded as innovative materials science based on light main-group metal oxides, which are widely used as the main ingredients for traditional ceramics, such as cement, glass and porcelain.

The function of materials is determined by the combination of elements and structures. Since the number of abundant elements is limited to 20–30, the key to realizing the ubiquitous element strategy is to find or create structures, as shown in figure 1. Important aspects of structures include bulk nanostructure, surfaces and interfaces, and defects, including non-conventional valence states. Materials scientists have a perception for each element based on their accumulated

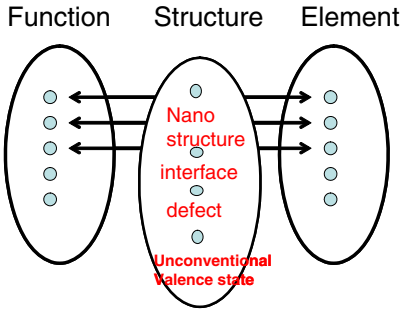

Order	Element
1	O
2	Si
3	Al
4	Fe
5	Ca
6	Na
7	K
8	Mg
9	H
10	Ti

Figure 1. Relation between element and function (left) and the list of 10 most abundant elements (right).

experience and knowledge. Realizing functionality that has been characteristic of a specific element by using a totally different element combined with an innovative structure is the essence of our strategy. A prerequisite to this approach is a deep understanding of the role of a key element in the material functionality in question. Novel information obtained from advanced characterization and theoretical modeling will be the platform for this understanding. Over the last decade, the science and technology of nanosized materials have advanced globally under widespread government and industrial support. The ubiquitous element strategy uses this accumulated knowledge to meet a real challenge of nano science and technology. The following subsections present two examples of past studies, which have provided important hints for the idea of the *ubiquitous element strategy*.

1.1. Conversion of a typical insulating oxide $12CaO \cdot 7Al_2O_3$ with a subnanometer-sized cage structure into a transparent conductor

A representative example to demonstrate the effect of nanostructures may be the observation of ferromagnetism and superconductivity in carbon nanotubes and fullerenes. Another case has been found in a traditional ceramic material, $12CaO \cdot 7Al_2O_3$ (C12A7), having a built-in nanostructure [1]. C12A7 is a stable compound of CaO and Al_2O_3, both of which are typical insulating oxides. It has a unique crystal structure composed of three-dimensionally connected, positively charged, subnanometer-sized cages, which are packed by sharing a monomolecular oxide layer. Free O^{2-} ions are present as the counter anions in two out of 12 cages in the unit cell to compensate the positive charge (+4 per unit cell) on the cage wall. Since the inner diameter of each cage is larger by $\sim 50\%$ than the diameter (0.28 nm) of O^{2-} ion, the O^{2-} ion is loosely coordinated by six Ca^{2+} ions within the cage wall. The free O^{2-} ions can be replaced by various anions, including active anion species that are unstable in a conventional environment. Figure 2 summarizes new functionalities realized in C12A7 by replacing the O^{2-} ion in the cage with O^-, H^- and e^-(electron).

C12A7 : O^- has a very high oxidation power, which can be used to oxidize Pt, whereas C12A7 : H^- is converted from insulator to electronic conductor upon ultraviolet illumination. Free O^{2-} ions in the cages can be directly replaced with electrons by chemical reduction treatment at high temperatures, and the resulting C12A7 : e^- may be regarded as an electride in which electrons serve as anions. This electride, which is chemically and thermally stable around room temperature, has a high conductivity of $\sim 1500\,S\,cm^{-1}$ and exhibits a metal–superconductor transition at 0.2 K.

The unique property of this material as a metal is its very low work function (2.4 eV), which is comparable to that of metallic potassium, combined with a chemically inert nature. Recent developments in electronic device applications that utilize these properties include cathodes of organic light-emitting diodes (OLEDs) electron field emitters and non-volatile memories; they are reviewed in section 2.

Three-dimensionally connected subnanometer-sized cages with a positive charge create a new conduction band, which is located at ~ 2 eV below the conduction band of the cage wall. This characteristic conduction band is called *cage conduction band* (CCB), and the origin of CCB is tunneling of an electron through the monomolecular oxide layer of the cage wall. The energy of the bottom of CCB is lower by ~ 2 eV than the bottom of the conduction band of CaO, which is comparable to that of the cage wall conduction band. C12A7 is converted from an insulator to a transparent semiconductor, metal and eventually superconductor, depending on the extent of exchange of O^{2-} and electrons. When C12A7 is heated in a dry O_2 or H_2 atmosphere, O^- and H^- ions become entrapped, respectively. The resulting C12A7 : O^- material exhibits high oxidation power, whereas a light-induced insulator–conductor transition is observed for C12A7 : H^-. It should be noted that the employed ingredients are very common compounds, namely CaO, Al_2O_3 and H_2O. Unique nanocages yielding CCB stabilize non-conventional active anion species, and various active functions atypical for these components are emerging from the resulting doped nanocages. This is a demonstration of hidden power of a nanostructure constituted from ubiquitous elements.

1.2. Giant thermoelectric response from the $SrTiO_3/TiO_2$ interface

Novel physical properties that are not expected in bulk phases can be observed at the surfaces and interfaces of ubiquitous-element compounds, which are usually chemically and electronically inactive in bulk phases. One example is a possible formation of metallic states at the (111) surface of rocksalt MgO. Our recent study of the nanoscale effects in MgO thin films are described in section 5. Here we review a study on the thermoelectric property enhancement using an interface created in $SrTiO_3$. That study shows a new path to save heavy elements, which are usually contained in conventional thermoelectric materials [2].

A discontinuity of chemical potential occurs at a sharp interface between different materials and results in a formation of a two-dimensional electron gas (2DEG). 2DEG

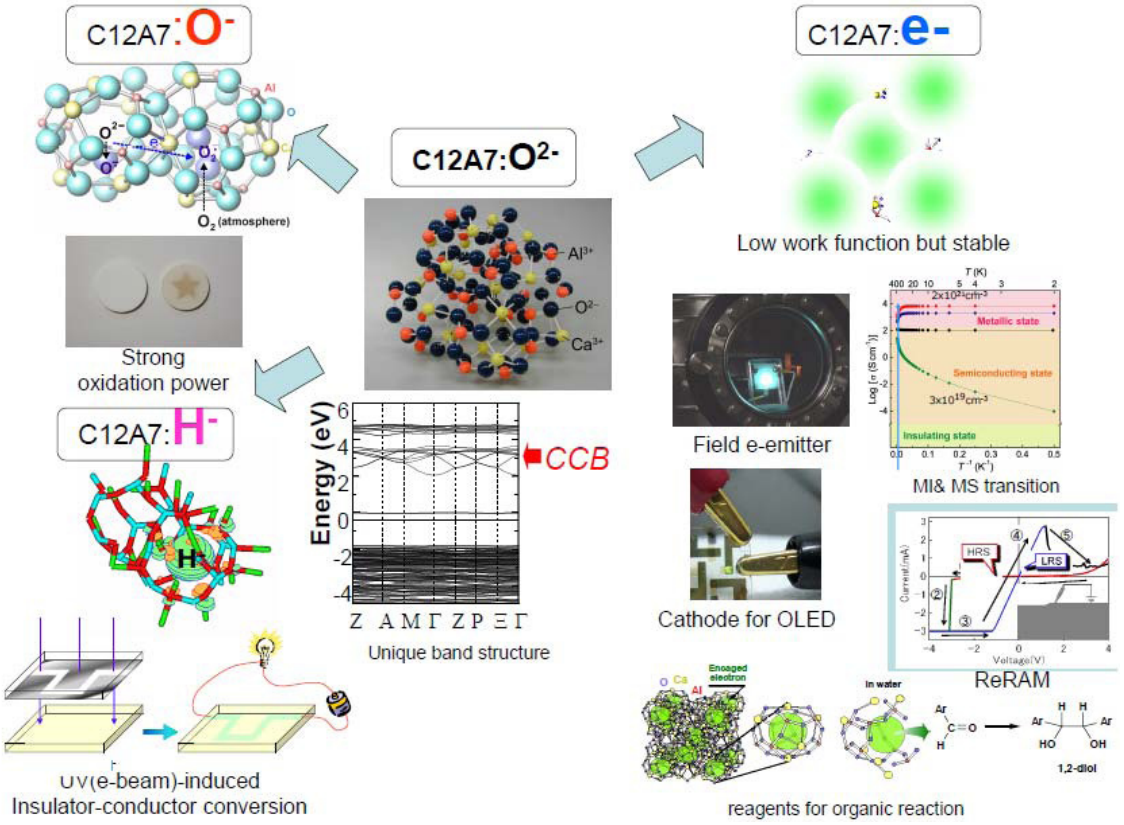

Figure 2. Active functionalities of $12CaO \cdot 7Al_2O_3$ (C12A7) realized by replacing O^{2-} ion in the crystallographic subnanometer-sized cages by abundant-anion species.

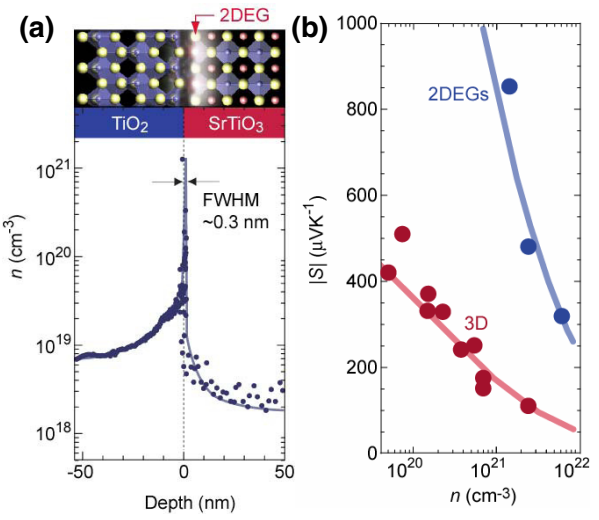

Figure 3. Large thermopower of 2DEG in a $SrTiO_3$ crystal. (a) Depth profile around the interface between a 56 nm thick TiO_2 (anatase) epitaxial film and the $SrTiO_3$ substrate. An strong carrier concentration peak ($n \sim 1.4 \times 10^{21}$ cm^{-3}) with a width of ~ 0.3 nm is observed at the $TiO_2/SrTiO_3$ interface. (b) $|S| - \log n$ plots for the 2DEGs and the $SrTiO_3$ bulk samples. The slope of $|S|$ for 2DEGs is about $-1000\,\mu$V K^{-1}, which is ~ 5 times greater than that for the $SrTiO_3$ bulk ($-198\,\mu$V K^{-1}).

exhibits different behavior from conventional electrons, such as high electron mobility. Figure 3 shows the Seebeck coefficient of the $SrTiO_3/SrTiO_3$: Nb interface as a function of thickness of TiO_2 layers epitaxially grown on bulk $SrTiO_3$. The Seebeck coefficient S at the interface is enhanced by a factor of ~ 5 compared with the bulk. This enhancement is due to the high density of the 2DEG formed at the sharp interface. The figure of merit (defined as $S^2\sigma T/\kappa$, where σ and κ are electrical and thermal conductivities) is as high as 2.4 at room temperature and is much higher than that of bulk Bi_2Te_3. This example shows a new route to realizing a high figure of merit using non-toxic and more common elements.

1.3. Content of this paper

The *ubiquitous element strategy* aims to achieve novel and/or useful functionalities, which have only been found in rare and/or harmful elements, with a restriction in selecting abundant and non-toxic elements for materials design. This article describes recent progress in this challenge. In section 2, we describe the application to optoelectronic devices of the C12A7 compound, which combines a low work function with a good chemical stability. Zirconia ceramic devices for efficient generation of atomic oxygen, which was conventionally produced using noble metals or high-energy devices, are reviewed in section 3. Control of fracture in mullite ($3Al_2O_3 \cdot 2SiO_2$) ceramics, which is another typical example of materials composed of the ubiquitous elements, by phase transitions and its application to a bumper shield for spacecraft is presented in section 4. In section 5, we describe a nanometer-scale control of MgO aiming to achieve

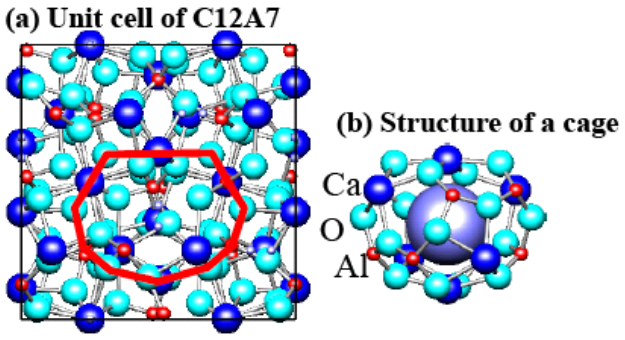

Figure 4. Crystal structure of C12A7: (a) unit cell and (b) a cage structure with a free oxygen ion (the large sphere) extracted from the red polygon in (a).

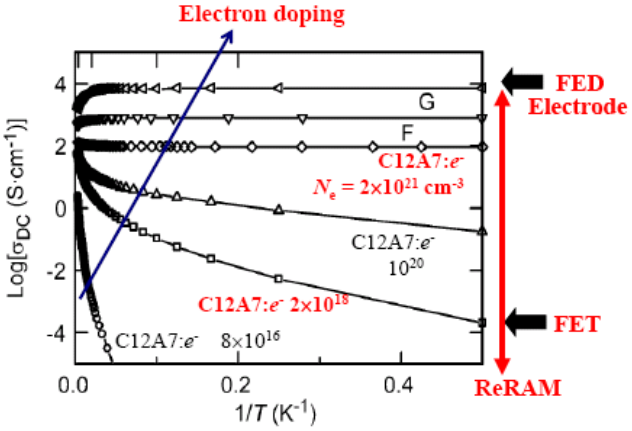

Figure 5. Temperature dependence of electrical conductivity of $C12A7:e^-$ with various electron densities in relation to their device applications. N_e is the mobile electron density at room temperature.

an artificial polar surface, and the concluding remarks are given in section 6.

2. Development of optoelectronic devices using a ubiquitous-element semiconductor, C12A7 : e$^-$

2.1. Introduction

As briefly explained above, C12A7 is a representative ubiquitous element material, because it exhibits a variety of electronic functions originating from its low work function (WF) of ~ 2.4 eV [3]. C12A7 is an oxide crystal with a naturally formed nanostructure, in which 12 subnanometer-sized cages are closely packed in a body-centered cubic unit cell [4] (figure 4). The cage framework $[Ca_{24}Al_{28}O_{64}]^{4+}$ is positively charged. Two O^{2-} ions, which are referred to as free oxygen ions, are confined in two of the 12 cages in the cubic unit cell, and thus the chemical composition of the unit cell is expressed as $[Ca_{24}Al_{28}O_{64}]^{4+}(O^{2-})_2$. It is possible to replace the free oxygen ions with other anions such as OH^- [5], F^- [6], Cl^- [6], O_2^- [7], O^- [8], H^- [9] and e^- [10]. C12A7 : H^- has a high electronic conductivity up to ~ 0.3 S cm^{-1} upon irradiation with ultraviolet (UV) light [9]. The density of mobile electrons (N_e) in C12A7 : e^- can be increased up to 2×10^{21} cm^{-3}, and the conduction changes from an insulating state ($\ll 10^{-12}$ S cm^{-1}) via intermediate semiconducting states, to a metallic state with a conductivity of ~ 1500 S cm^{-1} [10, 11] as shown in figure 5. Depending on the electron density and the corresponding carrier transport mechanism [3], [11–13], C12A7 : e^- materials are used for various optoelectronic devices, such as electron emitters [14, 15], field-effect transistors (FETs) [16–18], resistive random access memory (ReRAM) [19], and as an electron injection electrode for organic light-emitting diodes (OLEDs) [20, 21]. In this section, we review these optoelectronic applications of C12A7 : e^- in relation to its electronic structure and carrier transport mechanisms.

2.2. Low work function

The most interesting property of C12A7 : e^- is its low WF. Figure 6(a) shows a band structure of C12A7 : e^- calculated using density functional theory (DFT) [3, 22] in comparison with the simplified electronic structure of one of the constituents, CaO. Although DFT results do not provide an absolute energy level measured from the vacuum level (E_{vac}), we can estimate it from experimental results on CaO. Because the valence bands (VBs) of both C12A7 : e^- and CaO are mainly composed of O 2p orbitals, the absolute energy levels of their valence band maximums (VBMs) should be similar and may be aligned. Considering the bandgap and WF of CaO, it is expected that the Fermi level (E_F) of C12A7 : e^- is located ~ 3.7 eV below E_{vac}.

To confirm this prediction, we have attempted to measure the WF of C12A7 : e^- by photoemission spectroscopy (PES). However, reliable results could not be obtained by conventional soft x-ray PES (XPS) or UV PES (UPS) because they only probe the topmost surface layers where the bulk cage structure of C12A7 : e^- is not preserved. Therefore, we used hard x-ray PES (HAXPES) with an excitation energy of 7935.2 eV which penetrates deeper into the material [23]. The HAXPES results revealed that the VBM of C12A7 : e^- is located approximately 5.5 eV below E_F. From inverted PES (IPES), the conduction band minimum of the C12A7 frame is located approximately 2.0 eV above E_F, and thus the fundamental bandgap of C12A7 is about 7.5 eV. Using photoemission yield spectroscopy (PYS) we estimated the WF as 2.4 eV. This value is comparable to or even smaller than those of alkaline and alkaline-earth metals such as Na (2.8 eV), K (2.3 eV), Rb (2.2 eV), Cs (2.1 eV) and Ca (2.9 eV). Although the conventional low-WF metals are very reactive, in particular with atmospheric oxygen and water, C12A7 : e^- is very stable even in moist air and is more suitable for electronic devices. We attribute the combination of the low WF and chemical stability in C12A7 : e^- to its electronic structure in which the electrons at E_F are enclosed in the stable crystallographic cages which shield the electrons from reactions with environmental chemical species. This result strongly suggests that the separation of reactive electrons and a protective framework structure is a useful approach to design a new, stable, low-WF material.

We also observed a down-bending of the surface band in the UPS measurements. Such surface down-bending is

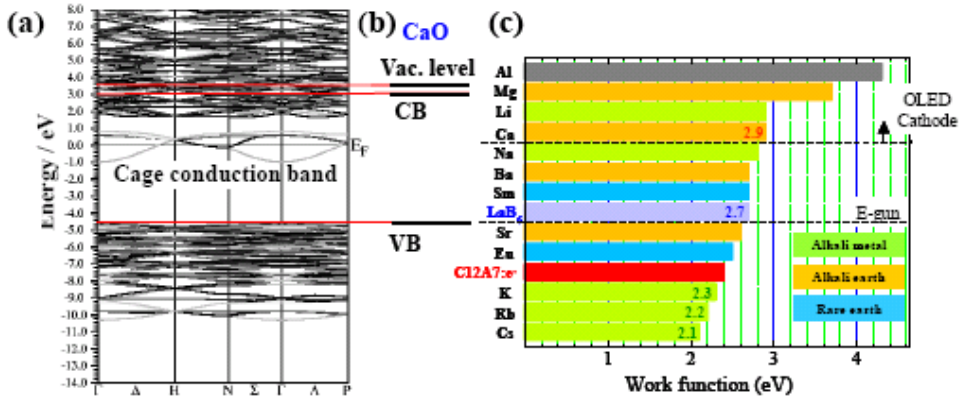

Figure 6. Electronic structure of highly doped C12A7 : e^-: (a) band structure of C12A7 : e^- calculated using density functional theory, (b) energy alignment with CaO by the valence band maxima and (c) work function of C12A7 : e^- in comparison with conventional low-work-function materials.

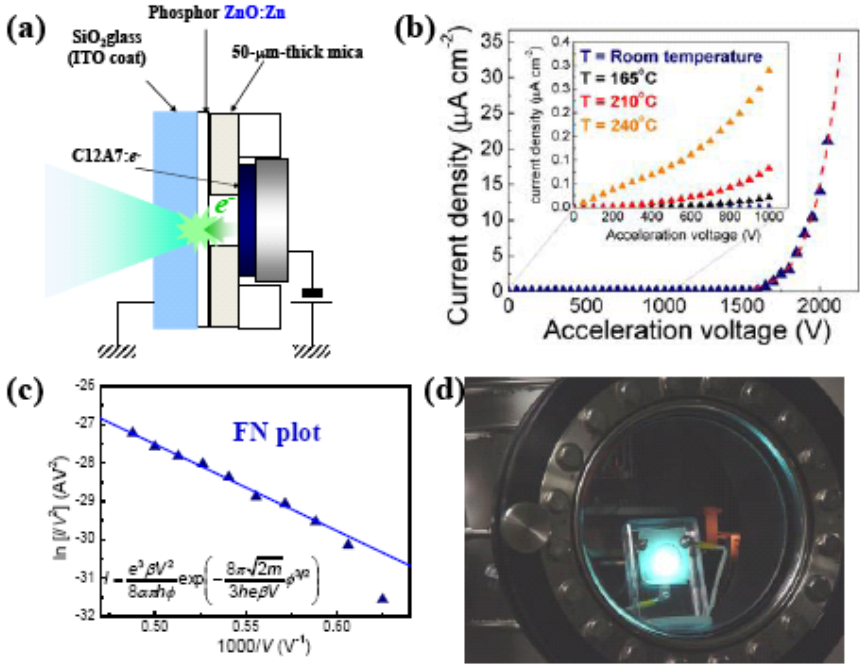

Figure 7. Electron emission from a flat surface of C12A7 : e^-: (a) device structure, (b) *I–V* characteristics at room temperature and other temperatures (inset). (c) Fowler–Nordheim (FN) plot of the data in (b). (d) Photo of a field emission device.

often observed in oxide semiconductors such as amorphous In–Ga–Zn–O [24] and is explained by a surface photovoltage effect in which holes are accumulated in the surface region, because the more mobile photoexcited electrons have diffused into the bulk faster than the holes [25].

2.3. Electron emitter

Chemically stable low-WF materials can find a variety of optoelectronic applications. A promising one is as an electron emitter, because electron emission from a solid is dominated by thermionic emission or Fowler–Nordheim (FN) field emission, and the emission threshold voltage increases with decreasing WF. Therefore, we investigated the fundamental electron emission properties of C12A7 : e^- using a mirror-polished C12A7 : e^- single crystal (figure 7) [14, 15]. As seen in figure 7(b), C12A7 : e^- began emitting electrons at a rather low voltage of 1700 V, and a high current density of approximately 25 μA cm^{-2} was obtained. The WF value of this emitter was estimated as 0.6 eV from the current-voltage (*I–V*) characteristics in the thermionic emission regime. This value is much lower than that obtained by PYS (2.4 eV).

In order to assess the fundamental properties of C12A7 : e^-, the above study was performed on a flat surface of C12A7 : e^-. However, a practical electron gun (e-gun) should employ a sharp emitter to enhance the electron emission current via the electric field concentration effect, and operate at an elevated temperature to stabilize the emission current (thermal field emission mode, TFE). Therefore, we fabricated an e-gun structure (figure 8(a)) in collaboration with Advantest Co. Ltd [15]. It was operated at rather low for a TFE temperatures, 650–900 °C, and its emission current

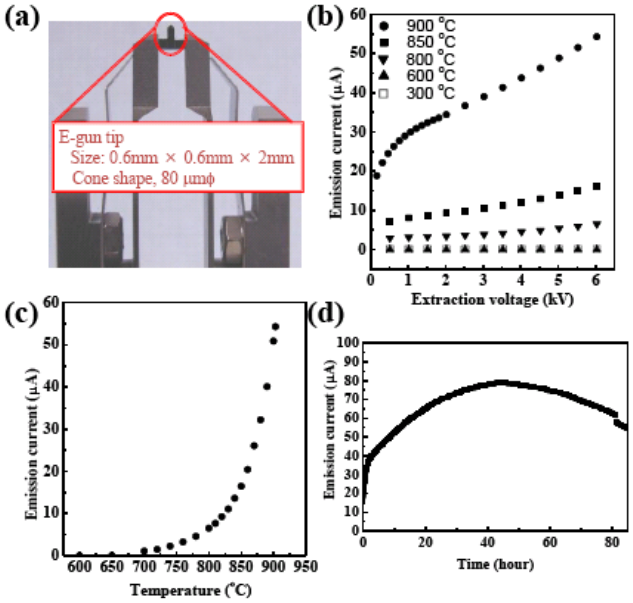

Figure 8. Electron emission using an electron-gun tip in the thermal field-emission regime: (a) device structure, (b) *I–V* characteristics at various temperatures, (c) emission current as a function of temperature at an extraction voltage of 6 kV, and (d) long-term stability of emission current at 900 °C; the extraction voltage of 6 kV was applied during the stability test.

reached 80 μA (1.5 A cm^{-2}). Although the emission current drifted with time, a high current density of $> 40\,\mu$A could be maintained for 80 h of continuous operation. The WF obtained from the thermionic emission characteristics in this case was ~ 2.1 eV, close to that obtained by PYS. These results indicate that the very low WF value of 0.6 eV obtained above was affected by the surface state, because the temperature in those measurements (figure 7) ranged between room temperature and 240 °C, whereas it reached 900 °C in other measurements, resulting in a cleaner surface of the e-gun tip.

2.4. Electron injection electrode for OLED

Another important application of a low-WF material is electron injection to optoelectronic devices. For example, organic semiconductors are mostly p-type and have small electron affinities (about 2.8–3.3 eV [26]). Therefore, electron injection to an organic layer is much more difficult than hole injection. This is one of the most serious issues affecting OLEDs; i.e. the operating voltage of the OLED is limited by the electron injection barrier (EIB) at the interface between the cathode and electron injection layer (EIL, figure 9). In conventional OLEDs, Al is used as the electron injection electrode because of its low WF among the stable metals, but it is usually combined with a buffer layer such as LiF to lower the EIB. Al was recently substituted by Mg that has a lower WF, and the high reactivity of Mg was suppressed by alloying.

We examined the use of C12A7 : e$^-$ as an electrode for electron injection into a representative organic semiconductor, Alq_3 [20, 21]. The WF of Alq_3 is 3.0 eV [26], that is larger than that of C12A7 : e$^-$; therefore, we expected that C12A7 : e$^-$ might form an ohmic contact with Alq_3. However, as mentioned above, the cage structure of C12A7 : e$^-$ is destroyed at the topmost surface that was even more pronounced in polycrystalline thin films of C12A7 : e$^-$ which we used. To improve the surface structure and the contact, we examined various post-deposition treatments including vacuum annealing, UV-O_3, Ar plasma and He plasma treatments. We found the He plasma treatment most efficient and obtained a small EIB value of 0.6 eV, less than half that of the best Al/LiF/Alq_3 interface reported to date [20] (figure 10).

We have also improved the hole injection electrodes. In conventional OLEDs, indium tin oxide (ITO) is used for this purpose, because it has a WF exceeding 5.0 eV despite ITO being a well-known n-type metallic conductor. However, to obtain a high WF, the surface of ITO should be oxidized, e.g. by oxygen plasma that increases the surface resistivity and the series resistance of the OLED. Therefore, we examined p-type inorganic metals and found LaCuOSe : Mg [27] and Cu_xSe [28], which gave almost linear *I–V* characteristics with low hole injection barriers (HIBs) of 0.3–0.4 eV to a representative hole injection material (HIM) *N*,*N*′-di-naphthalen-1-yl-*N*,*N*′-diphenyl-benzidine, about a half of the HIB reported for ITO (~ 0.6 eV).

Then, we developed OLED devices using C12A7 : e$^-$ as an electron injection electrode and Cu_xSe as a hole injection electrode. We employed an inverted OLED structure (figure 11(a)), in which a C12A7 : e$^-$ cathode is formed on a substrate and a Cu_xSe anode is located on top of the device, because high-temperature processes (crystallization at 1100 °C and reduction at 700 °C) are necessary to form the C12A7 : e$^-$ layer [29] and these cannot be applied to an organic device. Figure 11(b) compares the *I–V* and luminance–V (*L–V*) characteristics of OLEDs with a C12A7 : e$^-$ cathode and a conventional Al cathode [21]. It shows that the threshold voltage for light emission from the C12A7 : e$^-$-cathode device is around 6 V; it is lower than that for the conventional Al-cathode device because of the smaller EIB of C12A7 : e$^-$. Note that for both devices, the threshold voltages at which current starts flowing are much lower than the thresholds for light emission. The low thresholds for current flow are related to the low HIB and linear hole injection characteristics of the Cu_xSe anode.

2.5. Non-volatile memory utilizing fast oxygen ion conduction and insulator–conductor transition in C12A7

As mentioned above, the unit cell of C12A7 contains two free oxygen ions loosely encaged in subnanometer-sized cages, and these free oxygen ions can be extracted by chemical and physical treatments. This suggests that the free oxygen ions can easily migrate at high temperatures. Indeed, C12A7 is known as a fast ion conductor [30]. Therefore, we expect that applying an electric field to an insulating C12A7 : O^{2-} layer invokes oxygen ion conduction and removes the free oxygen ions, resulting in electron doping ('electric-field doping'). We also expect the diffusion constant of the oxygen ions to be very low at room temperature in the absence of electric field,

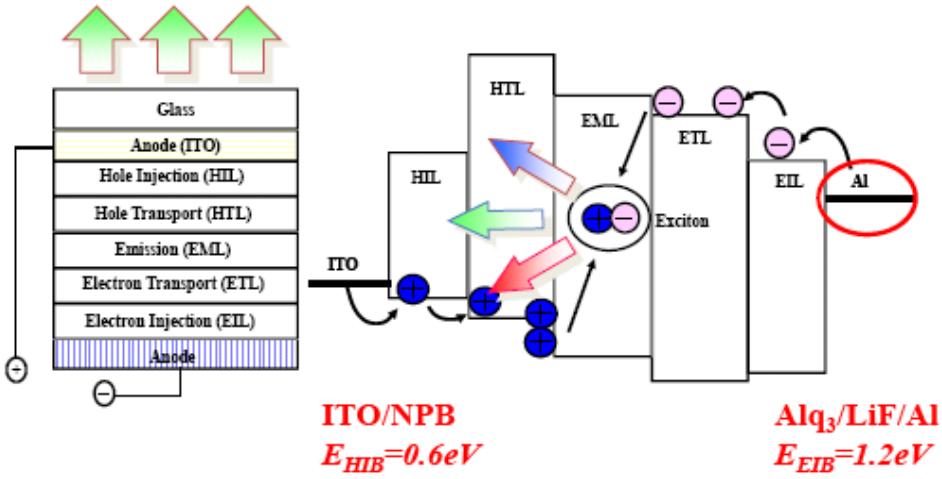

Figure 9. Schematic illustration of a typical device structure and electronic structure of an OLED.

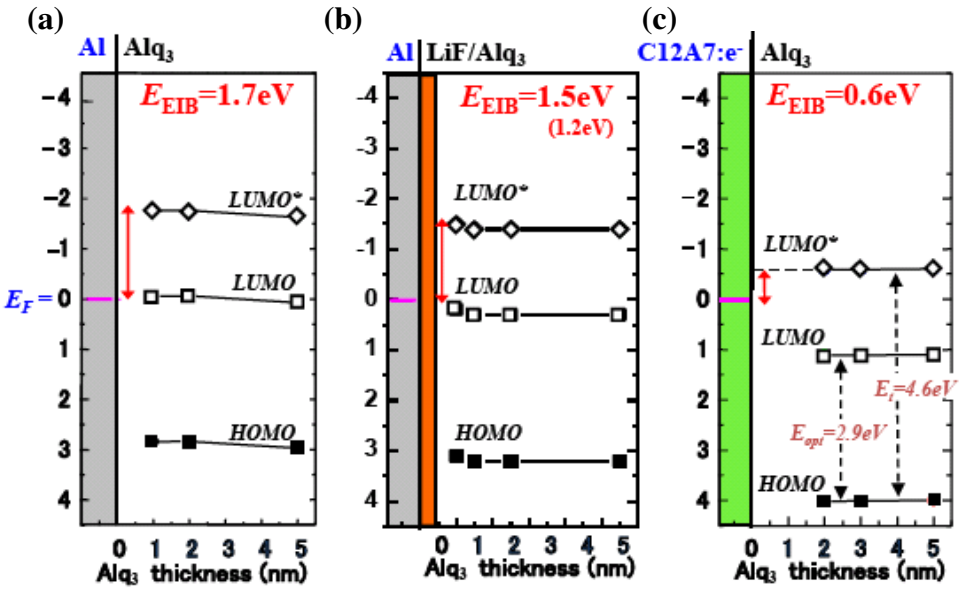

Figure 10. Electron injection barrier between (c) C12A7 : e^- and Alq_3 in comparison with conventional (a) Al and (b) Al/LiF electrodes.

suggesting that a new type of ReRAM could be realized using a C12A7 : O^{2-}/C12A7 : e^- stacked structure.

We fabricated such a structure as illustrated in figure 12(a) [19]. We used single-crystalline C12A7 : e^- as a starting material, which was synthesized by a Ti reduction treatment. The bottom Pt electrode was deposited by electron-beam (EB) evaporation, followed by annealing at 500 °C to form a better ohmic contact. The surface C12A7 : O^{2-} layer was formed by low-temperature oxidation. The thickness of the surface C12A7 : O^{2-} layer was estimated by spectroscopic ellipsometry as 50 nm after oxidation at 250 °C for 6 h in an oxygen flow. Finally, the top Pt electrode was formed by EB evaporation.

Figure 12(b) shows a typical *I*–*V* characteristic of the final device. When the bias voltage applied to the top Pt electrode was swept from 0 to negative values, the initial resistivity was very high (high resistivity state, HRS). When the negative bias exceeded a threshold voltage of about −3 V, the current jumped up and the resistivity switched to a low resistivity state (LRS). The LRS persisted even when the bias was swept toward positive voltages of up to 1 V. At higher voltages, the LRS changed into the initial HRS. We confirmed that this switching effect is reproducible for at least 50 times with the on-to-off resistivity ratios greater than 100 (figure 13). In other words, this device exhibited a bistable resistance switching effect and operated as a ReRAM.

2.6. Summary

C12A7 : e^- exhibits various electronic functions, although it is composed only of the abundant elements Ca, Al and O. The key to developing these functions is doping high electron densities into this wide bandgap (>7 eV) material, which results in the low WF and leads to applications as an electron emitter or an electron injection electrode for OLEDs. Another interesting phenomenon occurring in C12A7 is the insulator–conductor transition invoked by

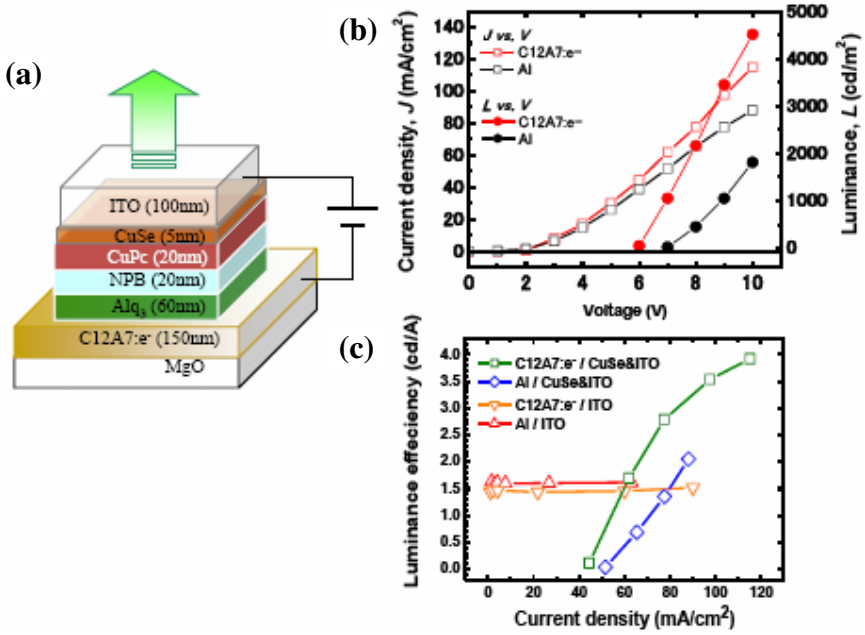

Figure 11. Inverted-structure OLED with a C12A7 : e^- electron injection electrode and Cu_xSe hole injection electrode. (a) device structure, (b) *I–L–V* characteristics and (c) luminance efficiency in comparison with those for conventional electrodes: Al cathode and ITO anode.

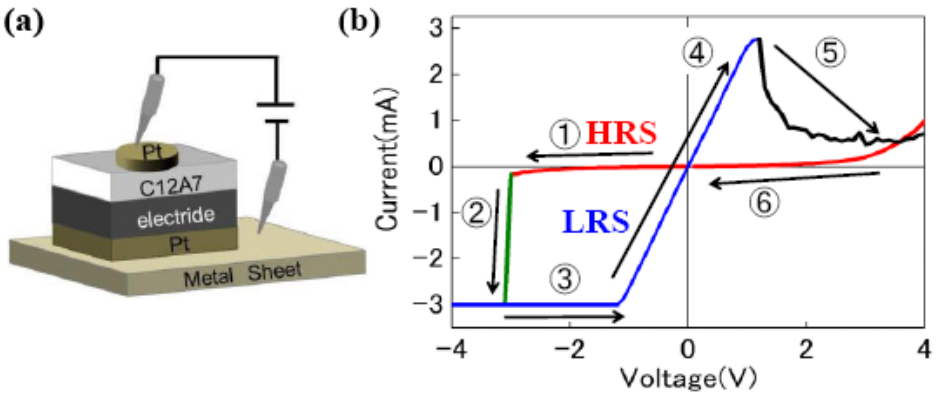

Figure 12. ReRAM based on a Pt/C12A7/C12A7 : e^- structure. (a) Device structure and (b) a typical *I–V* characteristic.

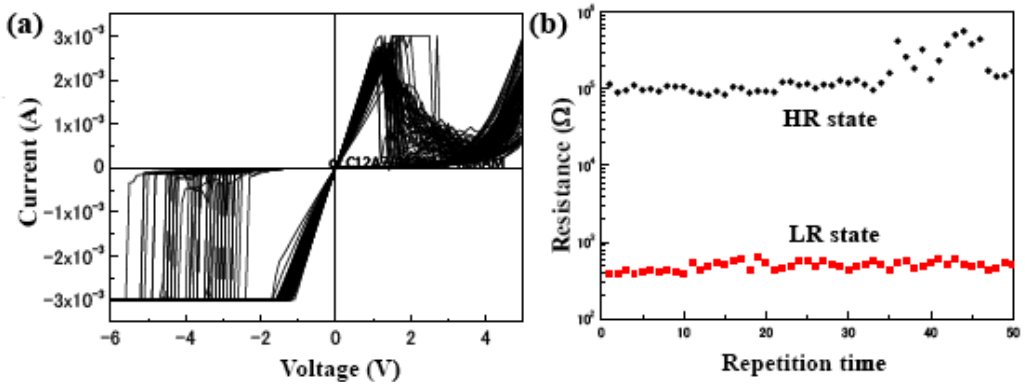

Figure 13. Repeated measurements of a C12A7/C12A7 : e^- ReRAM: (a) *I–V* characteristics and (b) resistivities in the HRS and LRS.

extracting the free oxygen ions from the subnanometer-sized cages. We demonstrated that a similar extraction and an insulator–conductor transition can be induced by electric field resulting in a non-volatile memory effect, which is assisted by the fast oxygen-ion conduction in C12A7. These features and the associated mechanisms are very different from those of conventional metals and semiconductors. In this sense, C12A7 : e^- is not just a ubiquitous-element material—it has

a great potential for developing new applications unavailable for conventional materials. Both the high-density electron doping to the wide bandgap material and the fast oxygen-ion conduction through the cages originate from the unique natural nanostructure of C12A7.

3. Atomic oxygen emission from zirconia at elevated temperatures

3.1. Introduction

Refractory materials retain their mechanical strength and chemical stability at high temperatures and are used as linings for furnaces, kilns and reactors. They are typically oxides of Si, Al, Ca, Mg, Zr or Ti. These elements are abundant, and hence exploring their new functionalities is an important step in establishing the concept of the *ubiquitous elements strategy*. C12A7 is also a constituent of a popular refractory material, alumina cement, which has been widely used as a castable lining. Its excellent thermochemical durability, particularly in severe reducing environments at elevated temperatures, enables changing it to an electrically active functional material [31, 32] by incorporating highly reducing species, H^- ion and electron, in the cages. In this section, a recent finding of new functionality in another refractory oxide is described, namely the efficient and selective generation of atomic oxygen (O) by zirconium oxide at high temperatures [33].

Molecular oxygen (O_2) is stable in ambient air. For it to become involved in an oxidation reaction, one must break its double bond that can be achieved even at room temperature by chemisorbing O_2 on a Pt surface [34]. The resulting 'atomic oxygen' plays a crucial role in the high activity of the Pt surface, which is found in practical devices such as automobile catalytic converters, polymer electrolyte fuel cells and so on. This makes Pt an important material in a wide range of industries, and its substitution is an important task of the ubiquitous element strategy.

Atomic oxygen is highly reactive; it easily abstracts hydrogen from organic molecules [35], inserts itself into C–H bonds [36], and etches polymer materials [37]. However its generation requires high energy [34]:

$$O_2(g) \rightarrow 2O(g): \quad \Delta H = 5.16\,\text{eV}. \tag{1}$$

Currently, a common method for generating atomic oxygen is extraction from gaseous plasma produced by exposing O_2 to radio- or microwave-frequency electric fields [38–40]. This process is complex, expensive and energy intensive; it generates spurious impurity ions, which may damage the product under fabrication. Thus, alternative methods for generating atomic oxygen have long been pursued [41–44].

Sections 3.2 describes how large quantities of atomic oxygen are selectively produced by incandescently heating an yttria-doped zirconia, a solid oxide electrolyte that conducts O^{2-} ions [33]. The main advantages of this approach over conventional plasma-based generation include higher energy efficiency, suppression of high-energy ionic species, operation in a wider pressure range, and elimination of high-frequency power sources, cooling systems and inert gases. This approach using a solid source offers a safe and versatile means of producing atomic oxygen. It allows producing silicon dioxide layers at lower temperatures compared to conventional processes as described in section 3.3.

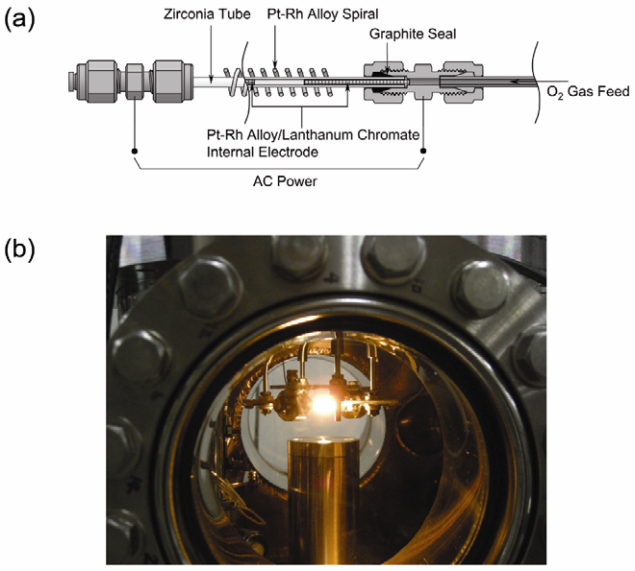

Figure 14. Schematic of the atomic oxygen emitter (a) and its operation in a vacuum system (b). The radiant part is the center of the zirconia tube in the assembly of (a). The metal cylinder is a quadrupole mass spectrometer (QMS).

3.2. Atomic oxygen emission from zirconia

In the solid-electrolyte source of atomic oxygen the electrolyte temperature is raised to 1400–1800 °C in vacuum using a Nernst lamp [45]. This old light-emitting device used a metal oxide filament, was about twice as efficient as carbon-filament lamps, did not require vacuum or noble gas atmosphere, and was successfully marketed around 1900. Solid electrolytes that exhibit high conductivity at elevated temperatures, including yttria-doped zirconia, arose in connection with the development of the Nernst lamp [46].

The emission device [33] is shown in figure 14. Two gas-permeable internal electrodes consisting of a thin wire of 87Pt-13Rh alloy and $La_{0.9}Sr_{0.1}CrO_{3-\delta}$ ceramics are separated by a 10 mm gap and located inside a polycrystalline $3\%Y_2O_3$-doped ZrO_2 ceramic tube with outer and inner diameters of 2.0 and 1.2 mm, respectively. The inside of the tube is sealed from the outside using graphite sealants and stainless steel gas inlets which are electrically connected to the internal electrodes. Oxygen gas at a pressure of 10−3000 Pa was supplied from one inlet, and the central region of the tube was heated to 1400–1800 °C by applying AC power to the electrodes. A spiral wire made of 87Pt-13Rh alloy was used as an auxiliary heater or as an extraction/suppression electrode for charged particles. Only a few tens of a watt was required to heat the zirconia tube in vacuum owing to its low thermal conductivity.

Quadrupole mass spectrometry (QMS) was used to analyze the particles emitted from the surface of zirconia tube

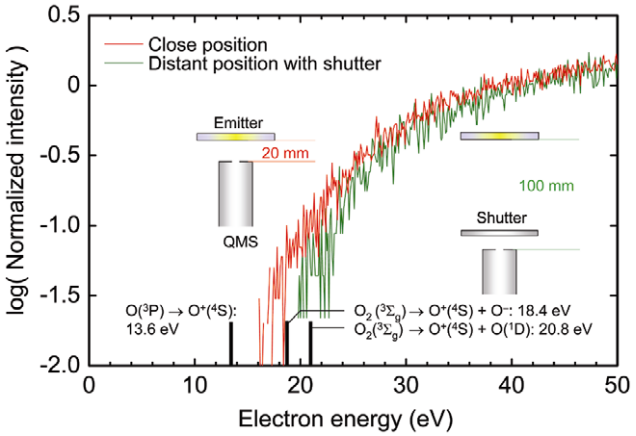

Figure 15. The number of O^+ ions plotted versus electron ionization energy. The red solid line was obtained when the QMS was placed near the hot zone and the green dashed line was obtained when the QMS was moved further away and a shutter was inserted. The data are normalized at 40 eV.

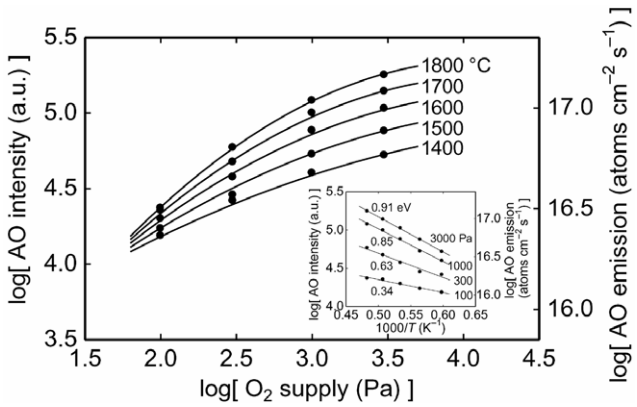

Figure 16. Variation of atomic oxygen emission intensity with the feed oxygen pressure and hot-zone temperature. The inset shows an Arrhenius plot. The right axes were calibrated by the absolute flux measurement using a quartz-crystal microbalance (QCM, see figure 17).

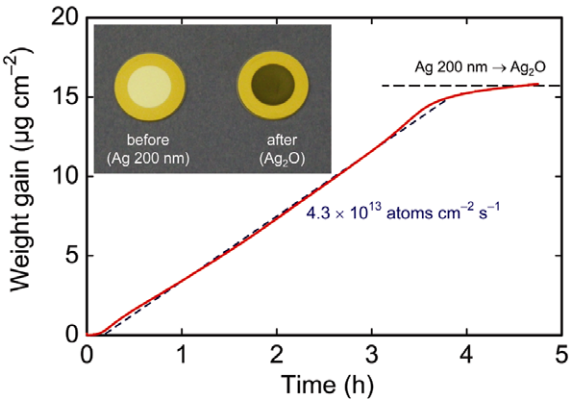

Figure 17. Weight change of a silver-coated QCM. The hot-zone temperature was 1700 °C. The oxygen pressure inside the zirconia tube was 3.0 kPa. The inset shows the QCM sensors before and after irradiation with atomic oxygen.

into the vacuum [33]. Atomic and molecular oxygen were separated using appearance potential spectroscopy [47–49], which characterizes a threshold energy for an electron impact ionization of a given particle. Figure 15 shows the spectra obtained when the spectrometer inlet was moved close to the hot zone (red line), and when the inlet was moved back to the distant position and a shutter was inserted (green line). The threshold electron energy for the ionization of atomic oxygen in the triplet ground state to generate an O^+ ion [$O(^3P) \rightarrow O^+(^4S)$] is 13.6 eV [47], while those for the dissociative ionization of O_2 are 18.4 eV [$O_2(X^3\Sigma_g^-) \rightarrow O^+(^4S) + O^-$] and 20.4 eV [$O_2(X^3\Sigma_g^-) \rightarrow O^+(^4S) + O(^1D)$] [48]. The signal below 18.4 eV is unambiguously attributed to atomic oxygen, enabling its detection without interference from the fragmentation of O_2. For the close-position case in figure 15, the O^+ signal is detected below 18.4 eV, clearly demonstrating the presence of atomic oxygen. In contrast, when the QMS is moved to the distant position and the shutter is inserted, the apparent threshold energy shifts to around 20 eV, indicating that this signal only originates from the dissociative ionization of O_2. The intensity of atomic oxygen emitted from the hot region of the zirconia surface tube decreased with increasing distance d approximately as $1/d^2$. Insertion of the shutter decreases the signal intensity to nearly zero. These observations suggest that the hot zone behaves like a point source of atomic oxygen.

Figure 16 shows the dependence of atomic oxygen intensity on the hot-zone temperature and the feed-oxygen pressure inside the tube. The emission intensity increases with either parameter. The average activation energy was 0.7 eV, which is considerably smaller than that observed for thermal O^- ion ($\sim 2.0-2.5$ eV) [50–55] and electron emissions (~ 6 eV) [56] from zirconia.

The absolute emission density of atomic oxygen from the hot zone was evaluated from the oxidation rate of a silver film deposited on a quartz-crystal microbalance (QCM) [33, 38] (figure 17). Inficon standard 6 MHz quartz crystals were freshly coated with a 200 nm thick silver layer by electron-beam evaporation. The QCM rate monitor was placed 11 cm away from the zirconia emitter. The temperature of the rate monitor was kept at 50 °C using a water circulator to minimize the effect of heat radiation and promote bulk diffusion in the (oxidized) silver film.

Silver does not react with O_2 near room temperature, although it traps atomic oxygen with a high probability [38] to be oxidized to Ag_2O. The atomic oxygen flux can be estimated from the slope of the weight gain. A nearly constant rate of weight gain indicates good stability in the emission flux. The total mass increase ($\sim 16\,\mu g\,cm^{-2}$) agreed well with that ($15.6\,\mu g\,cm^{-2}$) expected from full oxidation of silver to Ag_2O. This value gives the lower boundary for the actual atomic oxygen flux, because the atomic oxygen trapping efficiency of the silver coating is less than 100% and is believed to be a few tens per cent at room temperature. The value of 'irradiation flux' at the rate monitor was converted to that of 'emission flux' at the emission surface, assuming that it behaves as an isotropic point source, i.e. the flux decreases as $1/d^2$. The maximum emission flux was estimated as 10^{17} atoms $cm^{-2}\,s^{-1}$, which is equivalent to $2-20$ mA cm^{-2} of monovalent ion current and is comparable

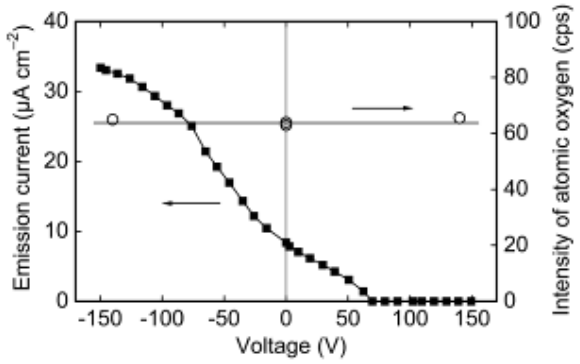

Figure 18. Effect of dc bias application. The open circles indicate the atomic oxygen emission intensity measured by QMS. The closed symbols represent an *I*–*V* characteristic for negative particle (electron and O^- ion) emission. The peak-to-peak voltage of the ac power supply was ±70 V. Note that the negative particle emission was completely suppressed above +70 V.

or higher than that of a typical plasma technique for the same energy injection levels (typically 10^{15-18} atoms s^{-1} at several hundred watts) [38–40].

To examine the effect of electric field, the internal zirconia electrodes were negatively biased. Figure 18 shows the dc bias voltage dependence of negative particle and atomic oxygen emission intensities. A weak negative charge emission was observed, which consisted of >95% electrons and <5% O^- ions. The emission current density was a few tens of $\mu A\,cm^{-2}$ at potentials of up to 150 V (an average electric field of 1.5 kV cm^{-1}). The negative particle flux was at least a few orders of magnitude lower than that of atomic oxygen. Furthermore, the negative particle emission was completely suppressed by applying a positive potential higher than the peak voltage of the ac power supply. In contrast, the emission intensity of atomic oxygen was independent on the bias and had no relevance to the negative particle emission.

The possible processes for atomic oxygen emission can be described with a general scheme for oxygen incorporation and desorption at the interface between a gas and metal oxide [57–60].

$$O_{2\,gas} \rightleftharpoons O_{2\,ads.} \rightleftharpoons O^-_{2\,ads.} \rightleftharpoons O^{2-}_{2\,ads.} \rightleftharpoons O^-_{2\,ads.\,or\,LC} \rightleftharpoons O^{2-}_{LC} \rightleftharpoons O^{2-}_{lat.}. \quad (2)$$

Here the subscripts indicate the gas phase, adsorbent, low-coordinated surface site and lattice sites. The O_2^{2-} ion on the *surface* is energetically unfavorable and even its general presence is controversial. Hence the interconversion between O_2^- and O^- ions is a candidate for the rate-determining step of oxygen incorporation and liberation [60].

According to this scheme, the desorption of oxygen species by the reduction of the metal oxide surface is initiated by a preferred hole trap of O^{2-} ions at low-coordinated surface sites, around defects such as step edges and vacancies, forming O^- ions. However, its direct desorption requires overcoming a large Coulomb interaction with the cation, the Zr^{4+} ion. The large reported activation energies for the O^- ion desorption (2.0−2.5 eV) [50–55] most likely correspond to the binding energy (figure 19) for the O^- ions to metal oxide

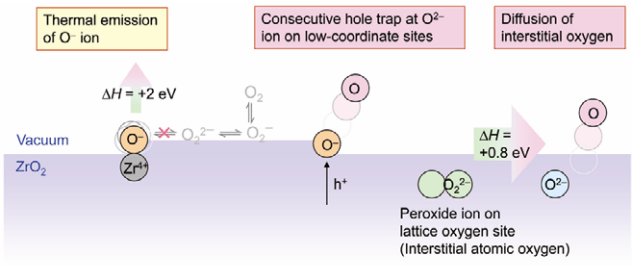

Figure 19. Possible atomic oxygen desorption processes from a zirconia surface.

surfaces. Coalescence of two O^- ions may then produce O_2^{2-} according to the above scheme. However, this process may be inhibited by a high energy barrier. Instead, we suggest that possible next steps are a disproportionation of two O^- ions to generate O and an O^{2-} ion ($2O^-_{ads.\,or\,LC} \rightarrow O^{2-}_{ads.\,or\,LC} + O_{gas}$), or a consecutive conversion of O^- into O, followed by desorption of atomic oxygen from the surface (figure 19).

Another candidate process for atomic oxygen desorption from the surface of zirconia is inferred from the enhanced formation of interstitial O in the ZrO_2 bulk as suggested by an experimental study on Si oxidation via an undoped ZrO_2 film [61] and a theoretical study on undoped ZrO_2 [62]. The theoretical calculation predicts that atomic oxygen is incorporated exothermally into the lattice with an energy gain of 0.8 eV, virtually forming an O_2^{2-} ion at the oxygen lattice site. Consequently, the minimum energy barrier for the atomic oxygen emission in vacuum from the *lattice* O_2^{2-} precursor is expected to be only 0.8 eV (figure 19). This value is comparable to that observed in our experiment, suggesting that the formation of O_2^{2-} is a possible origin for the atomic oxygen emission.

3.3. Formation of a thin oxide layer on silicon

Atomic oxygen is especially important in vacuum technology [38–44]. An instrument that produces a high flux of atomic oxygen would be useful in many applications, including fabrication of thin films of novel oxide materials [39, 43] and surface cleaning and modification in conjunction with surface analytical techniques. In this subsection, surface oxidation of Si is examined. Low-temperature formation of ultrathin oxide layers on semiconductors [63–65] is particularly important in the microelectronics industry for high-density device fabrication on glass or plastic substrates.

Silicon(100) substrates ($10 \times 10\,mm^2$; p-type; carrier density $\sim 10^{18}\,cm^{-3}$) were pretreated by the following process. They were cleaned in acetone and then in ethanol using an ultrasonic cleaner. Next the native oxide layer was removed by dipping in a 5% aqueous solution of hydrofluoric acid, followed by rinsing in ultrapure water, through which He gas was passed to remove dissolved oxygen. The irradiation with atomic oxygen was carried out with the source described in the previous section, at an oxygen supply pressure of 3.0 kPa and a hot zone temperature of 1700 °C. The atomic oxygen flux at the substrate position was estimated as

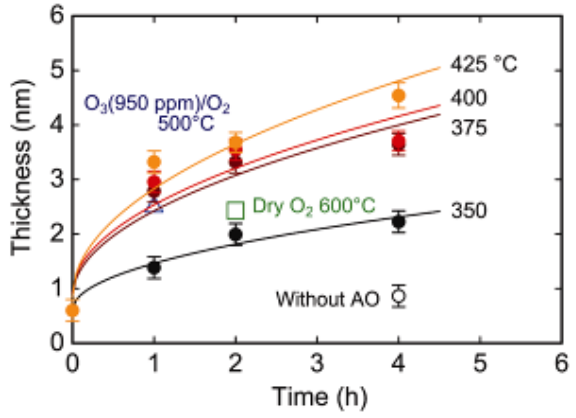

Figure 20. Growth of oxide layer on Si substrates under irradiation with atomic oxygen. Data for annealing in dry O_2 at 600 °C (green square) and in 950 ppm O_3 at 500 °C (brown triangle) [64] are added for comparison.

7×10^{14} atoms cm^{-2} s^{-1}. Background O_2 pressure in the chamber was 5×10^{-3} Pa. The substrate temperature was controlled at 350−425 °C, and the oxide thickness was measured by ellipsometry (Uvisel, Jobin Yvon).

Figure 20 shows the variation in the oxide thickness as a function of the substrate temperature and irradiation time. The thickness of the native oxide, which was formed after the cleaning process, was 0.6 nm, and was not changed by heating to 350 °C at the same background O_2 pressure (5×10^{-3} Pa) without the atomic oxygen irradiation. In contrast, the oxide growth was promoted markedly by the atomic oxygen irradiation. For comparison, the data for annealing in dry oxygen (100% O_2) at 600 °C and in ozone (950 ppm, O_2 balance) at 500 °C [64] are included in figure 20. The results indicate that the irradiation-assisted oxidation can yield the same oxide thickness as the thermal oxidation, but at a substrate temperature lower by a few hundred degrees.

The thickness-time dependences were fitted with a parabolic law:

$$d^2 = Bt, \tag{3}$$

where d is the thickness, t is time and B is the parabolic rate constant. The reasonable agreement between the fit and experimental data indicates that the oxidation rate was controlled by a bulk diffusion process. The temperature variation of the rate constant B (figure 21) is assumed to have an Arrhenius dependence:

$$B = C \exp\left(-\frac{E_a}{k_B T}\right), \tag{4}$$

where C is a constant and E_a is the activation energy. The value of E_a was estimated as 0.35 eV, which is only 1/4 of that for dry O_2 oxidation (1.34 eV) [66], indicating a significant promotion of the oxide growth by atomic oxygen. This value coincides with that for an oxidation process in concentrated (∼97%) O_3 [65]. In addition, a deviation from the Arrhenius dependence below ∼350 °C, which is probably due to a change in the rate-determining process, was also observed for the O_3 oxidation process. These similarities suggest that

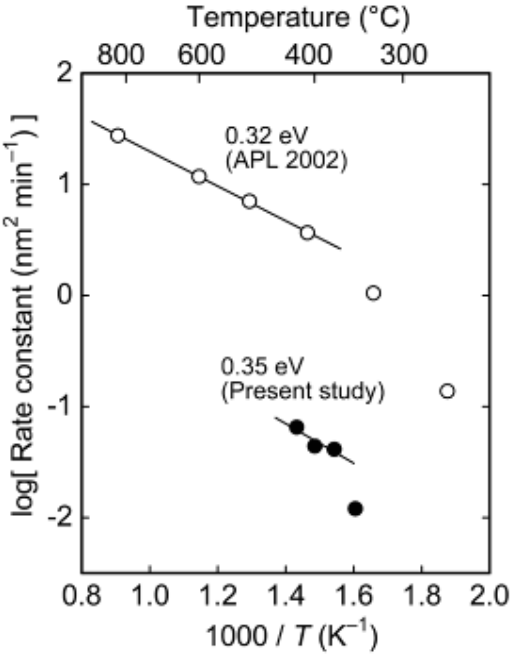

Figure 21. Arrhenius plot of the parabolic rate constants of the atomic oxygen irradiation process (present study) and of the O_3 process [65].

the same rate-determining process is responsible for the oxide layer growth in the atomic-oxygen and ozone-assisted processes. In the O_3 oxidation process, the relevant diffusion species has been assigned to atomic oxygen generated by the decomposition of O_3 on the substrate surface. This assignment is supported by the presented here results.

3.4. Summary

We have designed a generator of atomic oxygen by utilizing the general properties of refractory oxides, i.e. excellent durability at high temperature and large chemical potential gradient, together with the fast oxygen ion conductivity in zirconia. A zirconia tube (3% Y_2O_3-ZrO_2 with a 2.0 mm outer diameter) was incandescently heated in vacuum by direct application of electricity. Atomic oxygen emission from the hot surface was detected by appearance potential spectroscopy without interference from O_2. The atomic oxygen emission from zirconia is characterized by a few orders of magnitude higher intensity (∼10^{17} atoms cm^{-2} s^{-1}) and by a lower activation energy (∼0.7 eV) as compared to electron or O^- ion emission. This type of atomic oxygen source using solid oxide electrolytes has unique advantages over conventional plasma techniques including higher energy-efficiency, easier elimination of ionic species and possibility of operation in a wider pressure range. Irradiation with atomic oxygen using this source can reduce the temperature of the oxide growth on Si by a few hundred degrees as compared with thermal oxidation in dry O_2 or O_3 (950 ppm). This technique will find a wide range of applications particularly in the electronics industry.

4. Control of fracture in ceramics composed of 'ubiquitous elements' by phase transitions and its application to the Whipple bumper shield for spacecraft

4.1. Introduction

Construction and structural materials such as ceramics and concrete consist of abundant elements from the Earth's crust such as Si, Al, Fe, Ca, and most of these materials are oxides and hydroxides. Strength is crucial for their applications, and thus a lot of effort has been devoted to improving their mechanical properties. Some of these materials have peculiar characteristics, such as cage, layer and meso-porous structures, and the electrical and chemical properties of these materials have received considerable attention recently. The many reported functionalities of C12A7 ($Ca_{24}Al_{14}O_{44}^{4+}:4X^{-}$) make it a good example [8].

We propose to combine such features with the mechanical properties of structural materials aiming to develop new functionalities and applications. Since fracture and fragmentation of common materials are fundamentally important in everyday life, controlled fragmentation could be regarded as a kind of function (functional fragmentation). Ceramics are fragile under impact and blast-loading [67–69]. On the other hand, phase transitions can also be induced by impulsive shock-loading in many ceramics [70–72]. The use of structural phase transitions to control the fracture properties of ceramics may result in drastically improved materials for many applications concerning hyper-velocity impact, such as impact-resistant armor and the Whipple bumper shield for spacecraft.

We have reported the nano-order fragmentation (nanofragmentation) of mullite ceramics ($3Al_2O_3 \cdot 2SiO_2$) associated with a shock-induced disproportionation reaction [73]. Although mullite is a common high-temperature refractory material, shock compression (Hugoniot) measurements showed a phase transition at 30 GPa, which is interpreted as disproportionation to corundum and stishovite [74–76].

In accordance with the phase transition, transmission electron microscopy (TEM) observations of samples recovered after shock compression at 40–49 GPa revealed peculiar nanofragmentation [73]. Large crystallites of mullite, with a size of several micrometers, were broken into nanocrystallites smaller than 10 nm while preserving the original crystal orientation. Since this nanofragmentation occurred with an accompanying phase change, the mechanism of fracture must be associated with structural or compositional variations at the atomic level.

To clarify the mechanism of nanofragmentation, a comparative study was conducted with other aluminosilicates. Sillimanite ($Al_2O_3 \cdot SiO_2$) is a suitable material for comparison, because its crystal structure is very close to that of mullite [77]. Mullite is known to have non-stoichiometry in the Al_2O_3: SiO_2 ratio ranging from 3 : 2 to 2 : 1, and thus alumina-rich mullites are suitable materials for studying the effects of chemical composition, as they have similar crystal structures, but different amount of the oxygen vacancies. Polymorphous of sillimanite (kyanite and andalusite) were also studied to examine the effects of structure on nanofragmentation. A comparative study of these mullite-related aluminosilicates (mullite, alumina-rich mullite, sillimanite, andalusite and kyanite) was carried out using shock recovery experiments combined with x-ray diffraction (XRD), TEM and electron diffraction (ED) analyses [78]. The phase change behavior and microtextures of these materials varied widely, as discussed below.

Table 1. Transition pressures for the shock-induced amorphization of aluminosilicates.

Material	Alumina-rich mullite	Nominal mullite	Sillimanite	Andalusite	Kyanite
Transition pressure (GPa)	<30	30 [76]	38 [82]	46–52	>104*

*Partial disproportionation reaction to γ-alumina and silica has been observed.

Verification tests of mullite as a Whipple bumper shield material are presented as an example application of nanofragmentation [79]. Mullite showed superior protection ability, probably due to the high dynamic elastic limit, which enabled efficient fragmentation of the projectile. Furthermore, debris cloud fragments from the mullite bumper material were very fine, suggesting nanofragmentation even in the single-shield experiment.

4.2. Experimental details

Sintered specimens of polycrystalline mullite ($3Al_2O_3 \cdot 2SiO_2$) and alumina-rich mullite ($3.56Al_2O_3 \cdot 2SiO_2$) were provided by Nikkato Co. Ltd. Natural minerals were used for sillimanite, andalusite and kyanite. The samples were formed into pellets 14 mm in diameter and 1 mm thick, and then encased in an iron recovery capsule (diameter 22 mm, height 25 mm). Each recovery capsule was placed within a steel recovery fixture [80]. Impact experiments were performed using a two-stage light-gas gun at Tokyo Institute of Technology, using 3 mm thick Cu and Al flyer plates. Flyer velocity was measured using a magneto-flyer method, and the pressure in the recovery capsule was determined by an impedance match method [81]. The recovered samples were examined by XRD (RIGAKU Co. Ltd, MultiFlex) and 200 kV TEM (JEOL JEM-2000EX II).

4.3. Mechanism of nanofragmentation

Macroscopic phase changes of the recovered aluminosilicates were observed in the XRD patterns. In every aluminosilicate except kyanite (up to 104 GPa), crystalline to amorphous phase transitions were observed. The transition pressure to amorphous phase (table 1 [82]) and the ease of transformation increase with the amount of oxygen vacancies in the crystal structures. Only alumina-rich mullite, which has the highest amount of oxygen vacancies, could be completely amorphized.

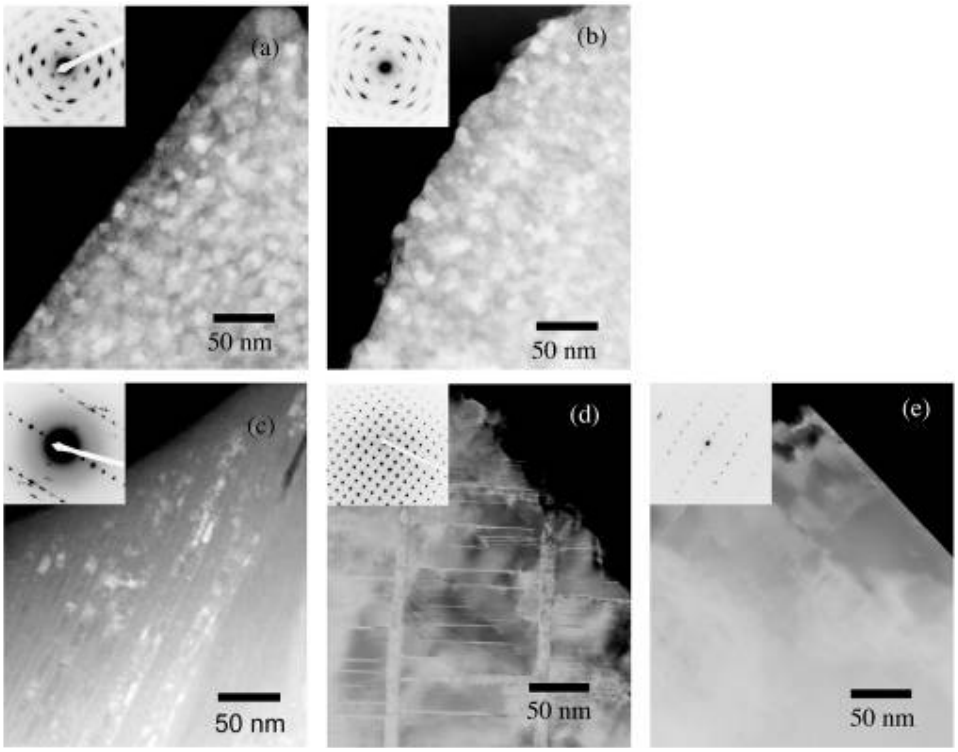

Figure 22. TEM images and corresponding electron diffraction patterns (inset) of shock-recovered samples of (a) mullite after 49 GPa, (b) alumina-rich mullite after 33 GPa, (c) sillimanite after 48 GPa, (d) andalusite after 52 GPa and (e) kyanite after 54 GPa.

Figure 22 shows typical TEM images with ED patterns in the insets, revealing a peculiar nanotexture with grains smaller than 10 nm in mullite (a) and alumina-rich mullite (b) compressed beyond the amorphization threshold. Only plastic deformation bands were observed for lower pressures (not shown). The nanotexture appears to be an aggregate of polycrystalline mullite. The lattice orientation of the nanocrystals was aligned, as indicated by the ED patterns, suggesting that the formed crystallites retained the crystal axis direction of the starting crystallites, and that instantaneous nano-order fragmentation in mullite and alumina-rich mullite occurred in association with the shock-induced phase transition.

The images of recovered samples of sillimanite (c) and andalusite (d) reveal coexistence of amorphous (bright) and crystalline (dark) phases. The ED pattern indicates that the lattice directions of the crystallites are closely aligned. This characteristic feature of shock-loaded sillimanite and andalusite was observed in naturally impacted sillimanite from the Ries Crater, Germany, by Stöffler *et al* and named 'planar deformation features (PDFs)' [83]. The textures observed in figures 22(c) and (d) are remnants of the very tiny ($\lesssim$10 nm) PDFs, and the amorphization of sillimanite and andalusite occurred along the PDFs. Such a feature is reminiscent of the well-known shock-induced amorphization of minerals, such as quartz or feldspar [84, 85]. Therefore, the mechanism for the amorphization of sillimanite and andalusite might be typical for other minerals, highlighting the importance of the nanofragmentation observed in mullite and alumina-rich mullite. Figure 22(e) shows a sample of kyanite recovered after compression at 56 GPa. Although the applied shock pressure was high enough to induce stacking faults and dislocations, almost no change in microtexture was observed. This means that the drastic changes in microtextures are associated with a macroscopic phase change, as was the case for sillimanite and andalusite.

Note that the peculiar nanofragmentation textures were only observed in mullite and alumina-rich mullite, which have oxygen vacancies in their crystal structures. In contrast, sillimanite, andalusite and kyanite have the same chemical composition (Al_2SiO_5) and contain no oxygen vacancies in their crystal structures. These results strongly suggest that the existence of the oxygen vacancies in the crystal is essential for the formation of the shock-induced nanofragmentation texture.

The crystal structures of mullite and sillimanite are very similar [77]. In sillimanite, edge-sharing Al^{3+} octahedral columns are connected in an ordered fashion by tetrahedral chains consisting of Al^{3+} and Si^{4+} ions. On the other hand, in mullite some of the Si^{4+} ions in the tetrahedral sites are replaced by Al^{3+} bringing disorder to the tetrahedral chains. Mullite has a non-stoichiometric alumina to silica ratio, and the amount of substitution, in $Al_2(Al_xSi_{1-x})O_{5-\delta}$ was $x = 0.25$–0.4. Considering the charge balance, there must be a random deficiency of oxide ions. In this study, the amount of oxygen vacancies δ was 0, 0.125 and 0.170 for sillimanite, mullite and alumina-rich mullite, respectively, and the amount of oxygen vacancies correlated with the progress of amorphization and the fragmented nanocrystallite size.

We have proposed that oxygen vacancies in mullite initiate amorphization upon compression, resulting in the

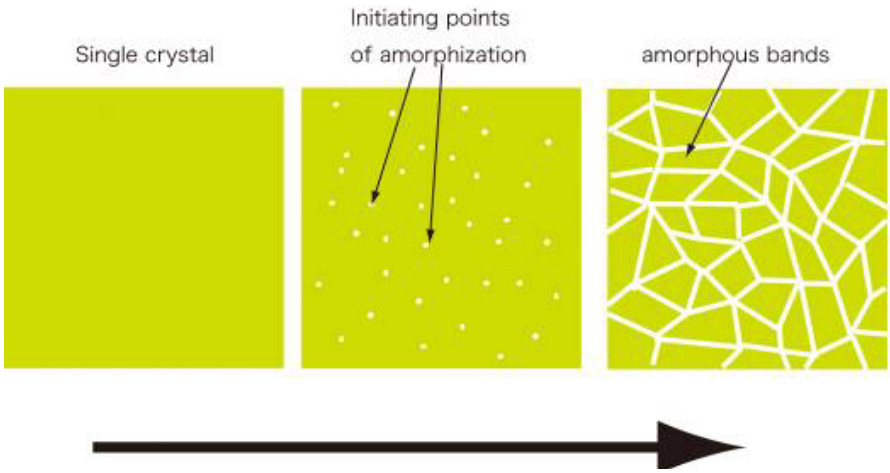

Figure 23. Proposed mechanism for nanofragmentation of mullite. The amorphization is triggered by a phase instability around the oxygen vacancies, which induces crystallographically uncontrolled crystal collapse and localized amorphization.

observed peculiar nanofragmentation [73, 78, 86]. As shown in figure 23, the amorphization of mullite is triggered by a phase instability around these oxygen vacancies, which results in the crystallographically uncontrolled crystal collapse and localized amorphization, as was demonstrated by a molecular dynamics simulation of pressure-induced amorphization originating at a point defect [87].

4.4. Application to the Whipple bumper shield

The results described above suggest the possibility of controlling dynamic deformation and fracture by a structural phase transition and/or chemical reaction, and that fine-tuning may be possible by careful selection of the chemical composition of the starting ceramic. As an example application of nanofragmentation, we conducted verification tests of mullite for a Whipple bumper shield material. The Whipple bumper shield is used to protect spacecraft from space debris or micrometeoroids flying at velocities of about 10 km s^{-1} by fracturing them upon impact [88, 89]. Mullite has a high dynamic elastic limit, and therefore its ability to fracture debris should be high. In addition, secondary debris from the bumper could form nano-order fragments because of the phase transition. These fragments would minimize damage to the spacecraft because mass and momentum of the secondary debris would be dispersed. These characteristics should enhance the performance of a Whipple bumper shield if mullite is used as a bumper material [90].

Figure 24 shows a schematic of the single-shield experiment. We used an aluminum alloy (Al6021P (JIS)) and mullite as bumper materials, for comparison. The bumper plate, 2 mm thick and 50 mm square, was located 100 mm from a witness plate made of an aluminum alloy block (Al2017P (JIS)), 50 mm thick and 200 mm square. The projectile consisted of an aluminum alloy plate (s2024Al (JIS)), 2 mm thick and 10 mm in diameter, mounted on a plastic sabot. The flyer plate and the sabot impacted the bumper together. After the impact of a projectile to a bumper plate, a debris cloud containing fragments of the projectile and bumper materials impacted the witness plate. The fracture

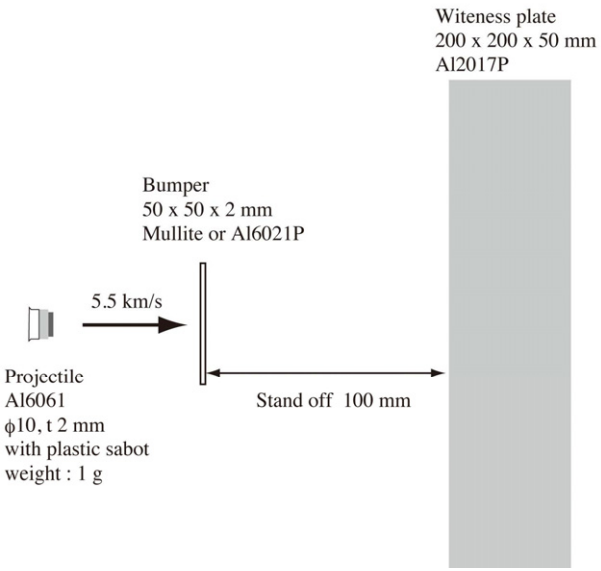

Figure 24. Schematic of the Whipple bumper shield experiment.

behavior and the protection efficiency of the bumper were estimated from the fracture pattern of the witness plate. In this study, one-dimensional crater depth profiles were measured, and the protection efficiency of the bumper was evaluated via the maximum crater depth.

Figure 25 shows impact crater patterns on the witness plates from the debris clouds of approximately 5.5 km s^{-1} impacts with mullite and aluminum alloy bumpers. The crater patterns consisted of a central area, mainly due to the primary debris fragments, and a fringe area, mainly due to the secondary debris fragments from the bumper. The damage in the central area was lower with a mullite bumper than with an aluminum alloy bumper indicating that the mullite bumper broke the projectile into smaller fragments than the aluminum bumper, and broke into smaller fragments itself. The maximum depth of the crater was much smaller with the mullite bumper than the aluminum alloy bumper. Also, the debris fragments were more dispersed with the mullite bumper, revealing its higher efficiency.

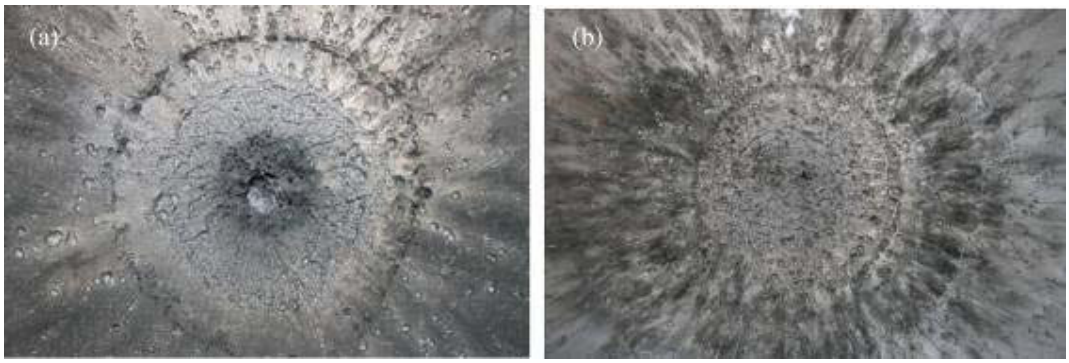

Figure 25. Impact crater patterns on the witness plates of (a) an aluminum alloy bumper impacted at 5.51 km s^{-1} and (b) a mullite bumper impacted at 5.61 km s^{-1}.

4.5. Summary

We have studied the mechanism of the peculiar nanofragmentation of mullite accompanying a phase transition induced by a shock wave. From the comparative study of the phase changes and microtextures of mullite-related aluminosilicates, we have proposed that oxygen vacancies in the crystal structure play an important role in the formation of the nanofragmentation texture. We have tested mullite as a material for the Whipple bumper shield of a spacecraft and found that mullite exhibited superior protection performance to the currently used aluminum alloy when tested for the impact by an aluminum alloy flyer at 5.5 km s^{-1}. These results suggest that dynamic deformation and fracture may be controlled by a structural phase transition and/or chemical reaction during the high-velocity impact.

5. MgO(111) thin films controlled at a nanometer scale

5.1. Introduction

The physical properties of surfaces and interfaces of ionic materials strongly depend on the morphology at an atomic scale. Atomic-scale control is particularly critical for polar surfaces and interfaces, which are present in many ionic materials including oxides [91–93]. Recently, a metallic interface phase has been found between polar and non-polar perovskite insulating oxides [94] and intensively studied to develop a new class of electronic devices. One of the simplest polar structures is the (111) film of metal monoxides with a rocksalt structure where oppositely charged 'cation-only layers' and 'anion-only layers' are alternately stacked along the [111]-direction. Growth of such a thin film along the [111]-direction results in a stacking of the metal^{2+}-O^{2-} dipole moments generating a diverging electrostatic potential. Thus the rocksalt (111) surface should be unstable when atomically flat. On the contrary, the rocksalt (100) surface is electrically neutral and hence stable.

MgO is a representative oxide insulator with a band gap of 7.8 eV [95]. MgO substrates and MgO(100) thin films have been widely used as insulating substrates for thin film growth and thin barrier layers, respectively. As shown in figure 26(a), the MgO(100) plane is

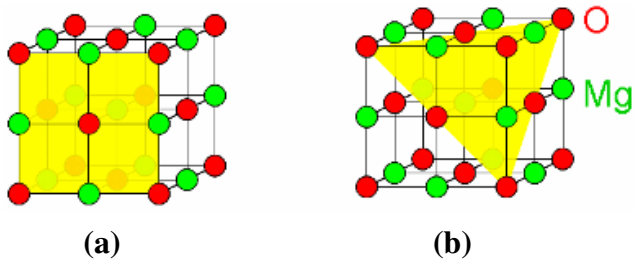

Figure 26. Crystal structure of MgO with shaded (100) (a) and (111) planes (b).

electrically neutral, like the bulk, and a band gap as large as about 6 eV was measured by scanning tunneling spectroscopy, even at a film thickness of three monolayers of MgO(100) [96]. On the other hand, the MgO(111) surface has attracted considerable theoretical attention as a representative polar surface [97–100]. It is, however, quite difficult to experimentally form an atomically flat MgO(111) surface. Recently, much effort has been spent to grow atomically flat MgO(111) films on Al_2O_3(0001) [101, 102], GaN(0001) [103], *6H*-SiC(0001) [104], and Ag(111) [105] substrates, and successful results were achieved only for Ag(111).

In this section, we review our recent growth studies of flat MgO(111) films on Al_2O_3(0001) [106] and on YSZ(111) with a NiO(111) buffer [107]. MgO(111) film growth on Al_2O_3(0001) is practically important because Al_2O_3(0001) is a common commercially available substrate. Film growth on NiO(111)-buffered YSZ(111) is critical for polar MgO(111) films, because it yields an atomically flat MgO(111) surface, which has not been available using other oxide substrates.

5.2. Fabrication of flat MgO(111) films on Al_2O_3(0001) substrates

α-Al_2O_3(0001) substrates have been commercially available and widely used to prepare thin films with hexagonal symmetry. The annealing conditions to prepare atomically flat α-Al_2O_3(0001) substrates have been established [108]. There are only few commercially available substrates for the growth of thin films with hexagonal symmetry, and thus the development of a flat MgO(111) buffer film on Al_2O_3(0001) should be rather valuable. The large lattice

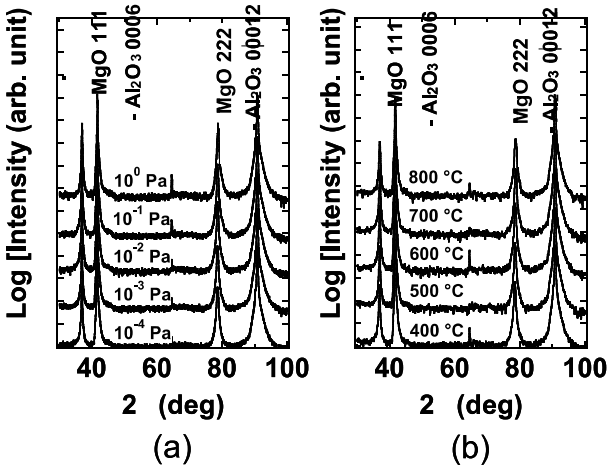

Figure 27. Out-of-plane XRD patterns of MgO films grown on Al_2O_3(0001) at 700 °C (a) under various oxygen partial pressures and (b) at various substrate temperatures under an oxygen partial pressure of 10^{-3} Pa. The characteristic forbidden Al_2O_3(0009) reflection is observed at ∼65° in some samples (reproduced with permission from [106] ©2009 The Japan Society of Applied Physics).

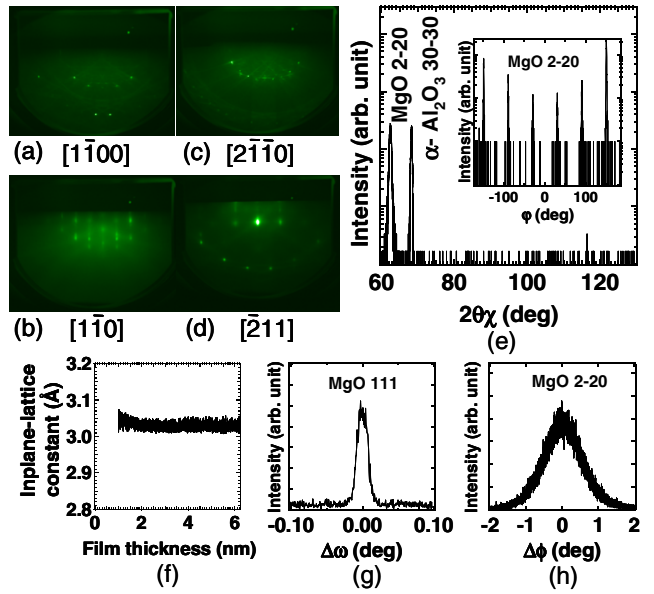

Figure 28. RHEED and XRD patterns of MgO films with a thickness of 70 nm grown at 700 °C under an oxygen partial pressure of 10^{-3} Pa. (a) (d) RHEED images with the electron beam incident along the (a), (b) [1$\bar{1}$00]-direction and (c), (d) [2$\bar{1}\bar{1}$0]-direction of the Al_2O_3(0001) substrates; (a) and (c) correspond to the Al_2O_3(0001) substrate before deposition and (b) and (d) correspond to the MgO film grown on Al_2O_3(0001). (e) In-plane XRD pattern parallel to the α-Al_2O_3 [30$\bar{3}$0]-direction. Inset: a ϕ scan rocking curve of the MgO(2$\bar{2}$0) diffraction, showing the sixfold rotational symmetry of the film. (f) In-plane lattice constant of the MgO(111) films monitored *in situ* by RHEED with the electron beam incident along the [1$\bar{1}$00]-direction. The film for this measurement was grown at a different repetition rate of 1 Hz. (g) Out-of-plane rocking curve for MgO(111). (h) In-plane rocking curve for MgO(2–20). (Reproduced with permission from [106] ©2009 The Japan Society of Applied Physics.)

constant difference between MgO and Al_2O_3 (8.3%) would facilitate deposition of other films. For example, a MgO(111) buffer layer, prepared by plasma-assisted molecular beam epitaxy (MBE), improves the quality of ZnO films grown on Al_2O_3(0001) substrates [101].

Although the band gap of MgO is larger than the energy of typical excimer lasers, pulsed laser deposition (PLD) has recently been successfully used to grow MgO films. While three-dimensional island growth was observed even at a monolayer thickness in MgO(111)/Al_2O_3(0001) films deposited by MBE [101], flat MgO(111) films were formed by PLD on Al_2O_3(0001).

We prepared atomically flat surfaces on α-Al_2O_3(0001) substrates by annealing at 1400 °C for 30 min in air [108]. MgO thin films were grown by PLD (Lambda Physik COMPexPro 201) using a MgO single-crystal target at a repetition rate of 10 Hz and a laser energy of ∼100 mJ incident to the chamber. The substrate temperature was between 400 and 800 °C and the oxygen partial pressure was between 10^{-4} and 1 Pa. The growth rate was 5.5–6.0 nm min^{-1} between 10^{-4} Pa and 10^{-2} Pa, 3.4 nm min for 0.1 Pa, and 1.4 nm min for 1 Pa.

The out-of-plane XRD patterns (figure 27) of the thus-prepared MgO films show the formation of (111) films under a wide range of growth condition. The film thickness was estimated with a profilometer as ∼60 nm for the samples grown under an oxygen partial pressure of 10^{-3} Pa and about 60–80 nm for all of the other samples.

The in-plane film-substrate epitaxial relationship was determined by reflection high-energy electron diffraction (RHEED) as shown in figures 28(a)–(d), where the [1$\bar{1}$0] and [$\bar{2}$11] directions of the MgO(111) films are parallel to the [1$\bar{1}$00] and [2$\bar{1}\bar{1}$0] directions of the Al_2O_3(0001) substrates, respectively. This in-plane relationship has been further confirmed by in-plane XRD measurements, as shown in figure 28(e). The out-of-plane and in-plane lattice constants of the 70 nm thick MgO(111) film were measured by high-resolution XRD as 4.215 and ∼4.20 Å, respectively, which are very close to the bulk value of rocksalt MgO (4.211 Å). The in-plane lattice constant was almost independent of the film thickness, as shown in the RHEED data of figure 28(f). Figures 28(g) and (h) reveal the full-width at half-maximum of the rocking curves as 0.019° (out-of-plane) and 1.3° (in-plane), respectively.

While transformation from the rocksalt phase for unsupported MgO(111) ultrathin films has been suggested before, according to first principle calculations [98, 100], the present MgO(111) films grown on Al_2O_3(0001) would remain in the rocksalt phase even at a film thickness of 1 nm, as the lattice constant remained unchanged. Similar behavior has also been observed for MgO/Al_2O_3(0001) films grown by MBE [102].

Atomic force microscopy (AFM) images revealed that a very flat surface of Al_2O_3(0001) survived even after deposition of a 60 nm MgO film, although valley-like structures were present for thicker films (figures 29(g) and (h)) in addition to the step and terrace structures. Figure 30(a) shows that the surface roughness estimated from the AFM scans weakly depends on the film thickness and remains as small as 0.62 nm even at a film thickness of

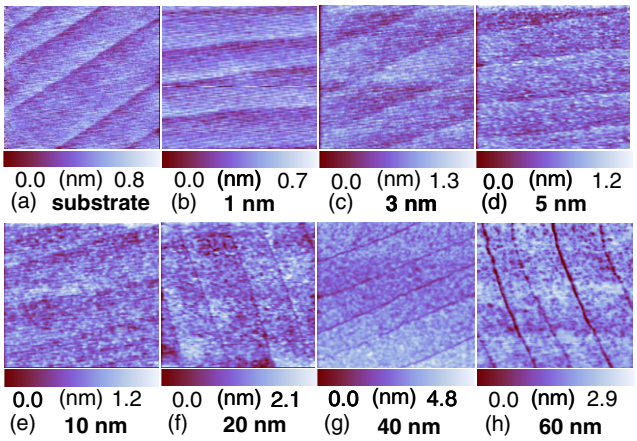

Figure 29. 1 μm^2 AFM images of (a) the Al_2O_3(0001) substrate and the MgO films grown on Al_2O_3(0001) at 700 °C under an oxygen partial pressure of 10^{-3} Pa with a film thickness of (b) 1, (c) 3, (d) 5, (e) 10, (f) 20, (g) 40 and (h) 60 nm. (Reproduced with permission from [106] ©2009 The Japan Society of Applied Physics.)

80 nm. In a simple diverging potential model, atomically flat surfaces of MgO(111) films should be roughened after deposition of only a few layers. The present observation indicates that relaxation mechanisms other than surface roughening or surface reconstruction must be present in MgO(111)/Al_2O_3(0001) films grown by PLD. As shown in figures 30(b) and (c), the surface roughness gradually increases with growth temperature and strongly increases with oxygen partial pressure. Note that a three-dimensional island growth mode has been observed for MgO(111) films deposited by MBE on Al_2O_3(0001) [102]. Since the kinetic energy of ablated species decreases with the oxygen partial pressure, the observed significant roughening at 1 Pa means that the kinetic energy of the ablated species is so small that the growth kinetics is similar to that of MBE, indicating that the high-energy growth process of PLD contributes to the formation of the flat polar surface.

5.3. Atomically flat MgO(111) surface formed on a YSZ(111) substrate with a NiO(111) buffer layer

In section 5.2, we have shown that MgO(111) films with relatively flat surfaces are formed on Al_2O_3(0001) substrates by PLD. However, an atomically flat surface has not been realized in MgO(111) films grown on any insulating or semiconducting substrate. Since the coexistence of a Mg plane and an O plane at the top (111) surface would significantly relax the polar instability even if the surface roughness remains on the subnanometer scale, the instability of MgO(111) films with relatively flat surfaces would be significantly smaller than that of atomically flat MgO(111) films. Here we have grown a MgO(111) film with an atomically flat surface on yttria stabilized zirconia (YSZ)(111) substrates with a NiO(111) buffer layer [106]. We have confirmed the atomically flat (111) surface by recording RHEED intensity oscillations during the film growth and by observing the single-step and terrace structure using AFM.

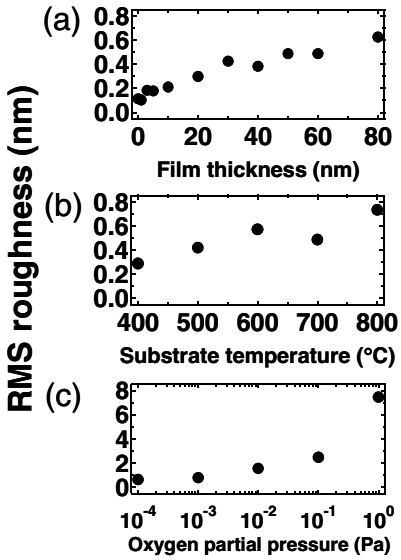

Figure 30. RMS roughness of the MgO(111) film surfaces: (a) thickness dependence for the films grown at 700 °C under an oxygen partial pressure of 10^{-3} Pa, (b) temperature dependence at an oxygen partial pressure of 10^{-3} Pa, and (c) oxygen partial pressure dependence at 700 °C. The film thicknesses are ~60 nm for (b) and 60–80 nm for (c). (Reproduced with permission from [106] ©2009 The Japan Society of Applied Physics.)

Both the NiO buffer layers and MgO films were grown by PLD using a KrF excimer laser with a MgO single-crystal target (4N purity) and a NiO sintered disk (3N purity). First we formed NiO(111) buffer films on YSZ(111) substrates at room temperature and an oxygen partial pressure $P_{O_2} = 1 \times 10^{-3}$ Pa using a laser power density of ~1.5 J cm^{-2}. Then we stacked two films face-to-face and annealed them in air at 1300 °C for 1 h to form single-crystalline NiO(111) films [109, 110]. After that we grew MgO thin films on these NiO buffer films. The substrate temperature (T_G) during the growth of MgO films was between 500 and 850 °C and P_{O_2} was between 10^{-4} and 5.0 Pa with a laser power density fixed at ~3.5 J cm^{-2}. RHEED patterns were recorded *in situ* with the electron beam incident along the [11$\bar{2}$] MgO direction.

Figures 31(a)–(c) show AFM images and cross-sectional profiles of the NiO substrate annealed at 1300 °C, a 20 nm thick NiO film on YSZ(111) and a 5-layer MgO(111) film on YSZ(111) with the 20 nm thick NiO buffer layer. Figure 31(b) shows the formation of an atomically flat NiO(111) surface with a single-NiO-layer step of 2.41 Å by annealing at 1300 °C. The film-substrate in-plane relationship was determined as [111] NiO ∥ [111] YSZ and [1$\bar{1}$0] NiO ∥ [1$\bar{1}$0] YSZ (data not shown) by high-resolution XRD measurements. For comparison, we annealed a commercial NiO(111) substrate at 1300 °C in air, at the conditions used to prepare the atomically flat surface of NiO(111)/YSZ(111), but found that many pits were formed as shown in figure 31(a). The MgO(111) atomically flat surface realized in the MgO(111)/NiO(111)/YSZ(111) structure is shown in figure 31(c), revealing a single-MgO-layer step (1 MgO layer corresponds to 2.43 Å) and a terrace structure. As MgO films are further deposited on the NiO(111)/YSZ(111) structure, the step and terrace structures gradually disappear, while

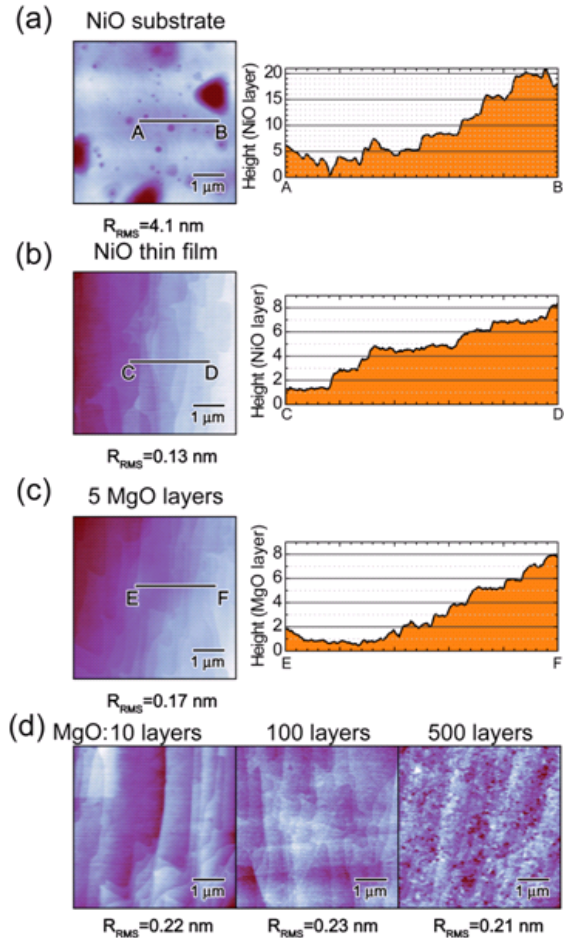

Figure 31. AFM images and cross sections (AB, CD and EF) of (a) NiO(111) single-crystal substrate annealed at 1300 °C, (b) 20 nm thick NiO(111) film grown on a YSZ (111) substrate annealed at 1300 °C and (c) 5 layers of MgO(111) grown on a YSZ(111) substrate with the 20 nm thick NiO(111) buffer layer. (d) AFM images of MgO(111) thin films of various thicknesses grown on a YSZ(111) substrate with the NiO(111) buffer layer. (Reproduced with permission from [107] ©2010 American Physical Society.)

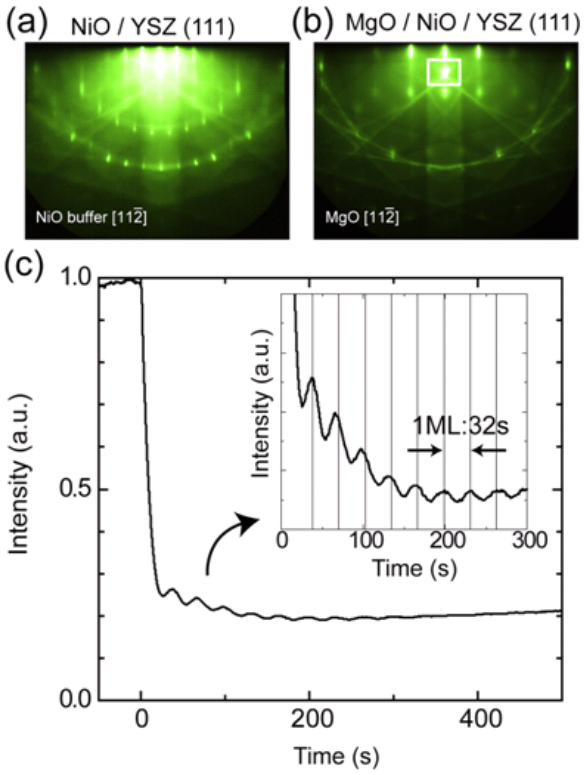

Figure 32. RHEED patterns of (a) NiO(111)/YSZ(111) and (b) 100-layer MgO(111) film grown on NiO/YSZ(111); 30 keV electrons were incident along the [11$\bar{2}$] azimuth of NiO or MgO. (c) RHEED intensity oscillations of the direct diffraction spot indicated by a rectangle in (b) during the MgO heteroepitaxial growth. The oscillations are magnified in the inset. (Reproduced with permission from [107] ©2010 American Physical Society).

the root mean square (RMS) surface roughness (R_{RMS}) was ~0.2 nm over a $5 \times 5\,\mu m^2$ area even at 500 MgO layers, which is very small compared with the values for MgO(111) films grown on GaN(0001) [103], 6*H*-SiC(0001) [104, 111] and α-Al_2O_3(0001) [111, 112]. Considering the strong instability of the MgO(111) polar surface, the realization of such a flat surface for a thick MgO(111) polar film is remarkable.

Figure 32(a) shows a RHEED pattern of a 20 nm thick NiO(111) film grown on a YSZ(111) substrate with a NiO(111) buffer layer, revealing a $p(2 \times 2)$ surface reconstruction [112–114]. While *local* formation of the atomically flat MgO(111) surface has been revealed by AFM, clear diffraction with Kikuchi lines indicates the presence of *an atomically smooth surface on a millimeter scale* corresponding to the spot size of the RHEED electron beam. Figure 32(c) shows that the intensity of specular RHEED diffraction oscillated for ~9 periods, consistent with the surviving step and terrace structure at 10 MgO(111) layers observed by AFM (figure 31(d)) for MgO growth at T_G = 600 °C and $P_{O_2} = 10^{-3}$ Pa on NiO(111)/YSZ(111). We have confirmed that the RHEED oscillation period (~32 s) in figure 32(c) corresponds to the thickness of one MgO layer with the rocksalt structure along the [111]-direction (2.4 Å) by grazing incidence x-ray reflectivity measurements. While the coexistence of a Mg plane and an O plane at the top (111) surface would be expected to significantly relax the polar instability, the observed RHEED oscillation shows that the present (111) surface is either O-rich or Mg-rich on a millimeter scale, where the polar instability would not be completely relaxed. Such RHEED oscillation was found over a wide range of growth conditions: T_G = 500–800 °C ($P_{O_2} = 10^{-3}$ Pa) and $P_{O_2} = 10^{-4}$–10^{0} Pa (T_G = 600 °C). It is remarkable that no significant surface reconstruction has been observed in the MgO(111)/NiO(111)/YSZ(111) structure. Figure 32(b) shows the RHEED pattern of a 100-layer MgO film deposited on a YSZ(111) substrate with a 20 nm thick NiO buffer layer. Its clear Kikuchi pattern indicates high film crystallinity and surface smoothness.

We have measured the in-plane and out-of-plane lattice constants of MgO films and characterized the NiO buffer layers by high-resolution XRD. The reciprocal space mapping around the asymmetric 402_{NiO} reflection of a 10-layer MgO(111) film shows that the in-plane

Table 2. Out-of-plane and in-plane lattice constants and stress relaxation rates of MgO(111) films of various thicknesses grown on a 20 nm thick NiO(111) buffer layer compared with the bulk MgO values. Lattice constants were determined from the asymmetric 402 reflection (Reproduced with permission from [107] ©2010 American Physical Society.)

	Out-of-plane		In-plane	
	d_{111} (Å)	d/d_0 (%)	$d_{1\bar{1}0}$ (Å)	d/d_0 (%)
MgO (45–0946)	2.432	–	2.978	–
MgO 10 layers	2.432	0.0	2.965	−0.4
MgO 100 layers	2.437	+0.2	2.965	−0.4
MgO 500 layers	2.436	+0.2	2.965	−0.4
NiO (47–1049)	2.412	–	2.954	–
NiO buffer layer	2.405	−0.3	2.965	+0.4

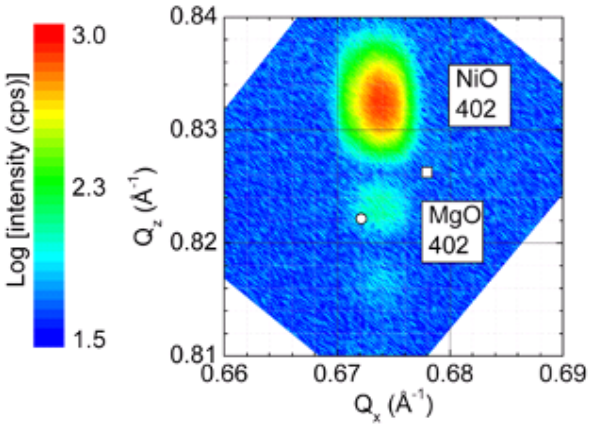

Figure 33. Reciprocal space mapping around the 402_{MgO} and 402_{NiO} reflections of a 10-layer MgO(111) film grown on NiO/YSZ(111). The circle and square indicate the bulk MgO and NiO values, respectively. (Reproduced with permission from [107] ©2010 American Physical Society.)

lattice constant of MgO films is locked to the value of the NiO buffer, independent of the MgO film thickness (figure 33), whereas the out-of-plane lattice constant does depend on the film thickness. Table 2 shows the lattice constants with stress-relaxation rates ($\Delta d/d_0$) for the MgO(111)/NiO(111)/YSZ(111) structure determined from the 402 reflection. The NiO film was −0.3% (out-of-plane) and +0.4% (in-plane) strained with respect to the bulk values. On the other hand, the 10-layer MgO film grown on a 20 nm thick NiO buffer layer was 0.0% (out-of-plane) and −0.3% (in-plane) strained with respect to the bulk values. As the MgO thickness was raised up to 100–500 MgO layers, the out-of-plane lattice constant increased by +0.2% with the in-plane lattice constant locked to the value of the NiO buffer layer. As mentioned above, the diverging energy of the polar stacking structure would be suppressed by an increase in the in-plane lattice constant, which would lower the two-dimensional charge density, and by a decrease in the out-of-plane lattice constant, which would reduce the electrode–electrode distance. Thus a slight decrease in the in-plane lattice constant and a slight increase in the out-of-plane lattice constant in our MgO(111) film are quite striking from the viewpoint of stacking polar structures.

Although the stabilization mechanisms are yet unclear [115][5], the realization of an atomically flat MgO(111) surface could have diverse implications: first, an atomically flat MgO(111) surface has never been prepared on any substrates except Ag(111). While the lattice constant of the MgO(111)/Ag(111) films differed significantly from the bulk MgO value, this was not the case for the MgO(111)/NiO(111)/YSZ(111) films, indicating the formation of an atomically flat surface of a polar *rocksalt* MgO(111) film. Such a film should be of great interest for applications considering that MgO is a key material in catalysis and nanoelectronics. Much effort has already been made to develop various functionalities using atomically flat MgO(100) surfaces and interfaces, and comparative studies of MgO(100) and (111) flat surfaces would provide a valuable insight.

5.4. Summary

We have grown relatively flat MgO(111) films on Al_2O_3(0001) substrates and atomically flat MgO(111) films on YSZ(111) substrates with NiO(111) buffer layers by PLD. In spite of the [111] polar direction, the surface of MgO(111) films grown on Al_2O_3(0001) remains rather flat with increasing film thickness. Together with commercial availability of Al_2O_3(0001) substrates with an atomically flat surface and the diverse applications of PLD to various oxides, the formation of flat MgO(111) films on Al_2O_3(0001) by PLD would be quite useful as buffer layers to grow thin films with hexagonal symmetry. Furthermore, using a YSZ(111) substrate with a NiO(111) buffer layer, we have realized the layer-by-layer growth of a MgO(111) thin film with an atomically flat surface, which has been studied theoretically for many years as a representative oxide polar structure. Since MgO is a key material in nanoelectronics and catalysis, the formation of the flat MgO(111) surface should trigger new applications of MgO.

6. Concluding remarks

This article briefly reviews our recent research performed within the ubiquitous element strategy summarized in figure 34. The primary interest of materials research up until the 1980 s was to find novel and efficient functionalities for the unexplored combinations of elements. The consequent rapid consumption of rare elements for high-tech products, driven by desire for increased living standards and explosive increase in population, along with the highly localized nature of rare-element deposits, has led to a supply crisis for rare elements, especially dysprosium, which is widely used in the strong Ne–Fe–B magnets for high-performance motors. This situation is similar to the 'oil crisis' of the 1970 s. That crisis was overcome by developing new technologies to enhance energy efficiency and provide alternative energy sources. The present 'rare-element' crisis is an undoubtedly serious issue for society but also a good opportunity to leap forward in

[5] A dominant role of hydrogen termination to stabilize the unreconstructed MgO (111) surface has been pointed out in [115].

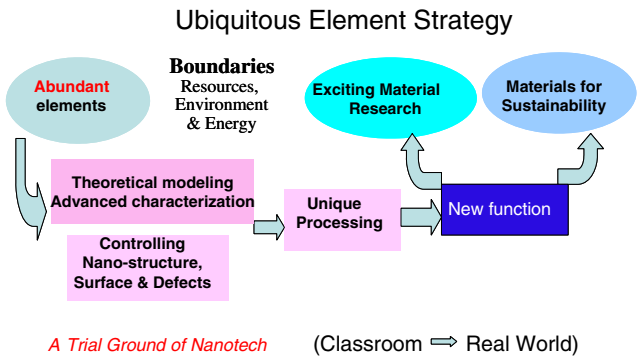

Figure 34. Outline of the ubiquitous element strategy in materials science.

materials science. The ubiquitous element strategy may be regarded as innovative materials science for a sustainable society. The new materials science needed to approach this tough issue may come from a fusion of various disciplines, such as chemistry, condensed matter physics and biology. The rapidly advancing fields of nano science and technology can provide the platform for this purpose. *Necessity is the mother of invention.* This old saying should also be true for the rare-element shortage.

Acknowledgment

This work was financially supported by the Ministry of Education, Culture, Sports, Science and Technology, Japan (Elements Science and Technology Project).

References

[1] Ginley D, Hosono H and Paine D 2010 *Handbook of Transparent Conductors* (Berlin: Springer) Chapter 10
[2] Ohta H *et al* 2007 *Nat. Mater.* **6** 128
[3] Toda Y, Yanagi H, Ikenaga E, Kim J J, Kobata M, Ueda S, Kamiya T, Hirano M, Kobayashi K and Hosono H 2007 *Adv. Mater.* **19** 3564
[4] Bartl H and Scheller T 1970 *Neues Jahrb. Mineral. Mon.* **35** 547
[5] Imlach J A, Glasser L S D and Glasser P F 1971 *Cement Concr. Res.* **1** 57
[6] Jeevaratnam J, Glasser F P and Glasser L S D 1964 *J. Am. Ceram. Soc.* **47** 105
[7] Hosono H and Abe Y 1987 *Inorg. Chem.* **26** 1192
[8] Hayashi K, Hirano M, Matsuishi S and Hosono H 2002 *J. Am. Chem. Soc.* **124** 738
[9] Hayashi K, Matsuishi S, Kamiya T, Hirano M and Hosono H 2002 *Nature* **419** 462
[10] Matsuishi S, Toda Y, Miyakawa M, Hayashi K, Kamiya T, Hirano M, Tanaka I and Hosono H 2003 *Science* **301** 626
[11] Kim S W, Matsuishi S, Nomura T, Kubota Y, Takata M, Hayashi K, Kamiya T, Hirano M and Hosono H 2007 *Nano Lett.* **7** 1138
[12] Sushko P V, Shluger A L, Hayashi K, Hirano M and Hosono H 2003 *Phys. Rev. Lett.* **91** 126401
[13] Sushko P V, Shluger A L, Hirano M and Hosono H 2007 *J. Am. Chem. Soc.* **129** 942
[14] Toda Y, Matsuishi S, Hayashi K, Ueda K, Kamiya T, Hirano M and Hosono H 2004 *Adv. Mater.* **16** 685
[15] Toda Y, Kim S W, Hayashi K, Hirano M, Kamiya T, Hosono H, Haraguchi T and Yasuda H 2005 *Appl. Phys. Lett.* **87** 254103
[16] Kamiya T, Aiba S, Miyakawa M, Nomura K, Matsuishi S, Hayashi K, Ueda K, Hirano M and Hosono H 2005 *Chem. Mater.* **17** 6311
[17] Nishio Y, Nomura K, Miyakawa M, Hayashi K, Yanagi H, Kamiya T, Hirano M and Hosono H 2008 *Phys. Status Solidi* A **205** 2047
[18] Nishio Y, Nomura K, Yanagi H, Kamiya T, Hirano M and Hosono H 2010 *Mater. Sci. Eng.* B **173** 37
[19] Adachi Y, Kim S W, Kamiya T and Hosono H 2009 *Mater. Sci. Eng.* B **161** 76
[20] Kim K B, Kikuchi M, Miyakawa M, Yanagi H, Kamiya T, Hirano M and Hosono H 2007 *J. Phys. Chem.* C **111** 8403
[21] Yanagi H, Kim K B, Koizumi I, Kikuchi M, Hiramatsu H, Miyakawa M, Kamiya T, Hirano M and Hosono H 2009 *J. Phys. Chem.* C **113** 18379
[22] Kamiya T, Ohta H, Hiramatsu H, Hayashi K, Nomura K, Matsuishi S, Ueda K, Hirano M and Hosono H 2004 *Microelectron. Eng.* **73–74** 620
[23] Kobayashi K *et al* 2003 *Appl. Phys. Lett.* **83** 1005
[24] Nomura K, Kamiya T, Ikenaga E, Yanagi H, Kobayashi K and Hosono H 2011 *J. Appl. Phys.* at press
[25] Würfel P and Würfel U 2009 *Physics of Solar Cells,* 2nd edn (New York: Wiley-VCH)
[26] Matsushima T *et al* 2007 *Chem. Phys. Lett.* **435** 327
[27] Yanagi H, Kikuchi M, Kim K B, Hiramatsu H, Kamiya T, Hirano M and Hosono H 2008 *Org. Electron.* **9** 890
[28] Hiramatsu H, Koizumi I, Kim K B, Yanagi H, Kamiya T, Hirano M, Matsunami N and Hosono H 2008 *J. Appl. Phys.* **104** 113723
[29] Miyakawa M, Hirano M, Kamiya T and Hosono H 2007 *Appl. Phys. Lett.* **90** 182105
[30] Lacerda M, Irvine J T, Glasser F P and West A R 1988 *Nature* **332** 525
[31] Hayashi K, Hirano M and Hosono H 2007 *Bull. Chem. Soc. Japan* **80** 872
[32] Kim S-W, Matsuishi S, Miyakawa M, Hayashi K, Hirano M and Hosono H 2007 *J. Mater. Sci. Mater. Electron.* **18** S5
[33] Hayashi K, Chiba T, Li J, Hirano M and Hosono H 2009 *J. Phys. Chem.* C **113** 9436
[34] Gland J L, Sexton B A and Fisher G B 1980 *Surf. Sci.* **95** 587
[35] Luntz A C 1980 *J. Chem. Phys.* **73** 1143
[36] Cetanović R J 1987 *J. Phys. Chem. Ref. Data* **16** 261
[37] Packirisamy S, Schwam D and Litt M H 1995 *J. Mater. Sci.* **30** 308
[38] Matijasevic V, Garwin E L and Hammond R H 1990 *Rev. Sci. Instrum.* **61** 1747
[39] Locquet J P and Mächler E 1992 *J. Vac. Sci. Technol.* A **10** 3100
[40] Ingle N J C, Hammond R H, Beasley M R and Blank D H A 1999 *Appl. Phys. Lett.* **75** 4162
[41] Davidson M R, Hoflund G B and Outlaw R A 1993 *Surf. Sci.* **281** 111
[42] Hoflund G B and Weaver J F 1994 *Meas. Sci. Technol.* **5** 201
[43] Wisotzki E, Balogh A G, Hahn B, Wolan J T and Hoflund G B 1999 *J. Vac. Sci. Technol.* A **17** 14
[44] Kinoshita H, Ikeda J, Tagawa M, Umeno M and Ohmae N 1998 *Rev. Sci. Instrum.* **69** 2273
[45] Nernst W 1901 US-P 685 730 filed 24.8.1899
[46] Mobius H H 1997 *J. Solid State Electrochem.* **1** 2
[47] Moore C E 1949–1958 *National Bureau of Standards Circular* No. 467, Vol III (Washington, DC: U. S. Government Printing Office)
[48] Homer D H 1951 *Rev. Mod. Phys.* **23** 185
[49] Agarwal S, Quax G W W, van de, Sanden M C M, Maroudas D and Aydil E S 2004 *J. Vac. Sci. Technol.* A **22** 71

[50] Nishioka M, Torimoto Y, Kashiwagi H, Li Q and Sadakata M 2003 *J. Catal.* **215** 1
[51] Nishioka M, Nanjyo H, Hamakawa S, Kobayashi K, Sato K, Inoue T, Mizukami F and Sadakata M 2006 *Solid State Ionics* **177** 2235
[52] Fujiwara Y, Kaimai A, Hong J-O, Yashiro K, Nigara Y, Kawada T and Mizusaki J 2003 *J. Electrochem. Soc.* **150** E117
[53] Sakai T, Fujiwara Y, Kamimai A, Yashiro K, Matsumoto H, Nigara Y, Kawada T and Mizusaki J 2006 *J. Alloys Compounds* **408–412** 1127
[54] Li Q, Hayashi K, Nishioka M, Kashiwagi H, Hirano M, Torimoto Y, Hosono H and Sadakata M 2002 *Appl. Phys. Lett.* **80** 4259
[55] Li J, Hayashi K, Hirano M and Hosono H 2009 *J. Electrochem. Soc.* **156** G1
[56] Rifflet J C, Odier P and Anthony A M 1975 *J. Am. Ceram. Soc.* **58** 493
[57] Manning P S, Sirman J D and Kilner J A 1997 *Solid State Ionics* **93** 125
[58] Panov G I, Uriarte A K, Rodkin M A and Sobolev V I 1998 *Catal. Today* **41** 365
[59] Nowotny J, Bak T, Nowotny M K and Sorrell C C 2005 *Adv. Appl. Ceram.* **104** 147
[60] Merkle R and Maier J 2002 *Phys. Chem. Chem. Phys.* **4** 4140
[61] Busch B W, Schulte W H, Garfunkel E and Gustafsson T 2000 *Phys. Rev.* B **62** R13290
[62] Foster A S, Sulimov V B, Lopez GejoF, Shluger A L and Nieminen R M 2001 *Phys. Rev.* B **64** 224108
[63] Kazor A and Boyd I W 1993 *Appl. Phys. Lett.* **63** 2517
[64] Cui Z, Madsen J M and Takoudis C G 2000 *J. Appl. Phys.* **87** 8181
[65] Nishiguchi T, Nonaka H, Ichimura S, Morikawa Y, Kekura M and Miyamoto M 2002 *Appl. Phys. Lett.* **81** 2190
[66] Ng K K, Polito W J and Ligenza J R 1984 *Appl. Phys. Lett.* **44** 626
[67] Bourne N, Millett J, Rosenberg Z and Murray N 1998 *J. Mech. Phys. Solids* **46** 1887
[68] Grady D E 1998 *Mech. Mater.* **29** 181
[69] Chen M W, McCauley J W, Dandeker D P and Bourne N K 2006 *Nat. Mater.* **5** 614
[70] Sekine T, He H L, Kobayashi T, Zang M and Xu F F 2000 *Appl. Phys. Lett.* **76** 3706
[71] Atou T, Kusaba K, Fukuoka K, Kikuchi M and Syono Y 1990 *J. Solid State Chem.* **89** 378
[72] Syono Y, Kusaba K, Atou T and Fukuoka K 1992 *Shock Waves* ed K Takayama (Berlin: Springer) p 121
[73] Kawai N, Atou T, Ito S, Yubuta K, Kikuchi M, Nakamura K G and Kondo K 2007 *Adv. Mater.* **19** 2375
[74] Aksay I A, Dabbs D M and Savikaya M 1991 *J. Am. Ceram. Soc.* **74** 2343
[75] Schneider H, Okada K and Pask J 1994 *Mullite and Mullite Ceramics* (New York: Wiley)
[76] Kawai N, Nakamura K G and Kondo K 2004 *J. Appl. Phys.* **96** 4126
[77] Deer W A, Howie R A and Zussman J 1982 *Orthosilicates* Vol. 1A (London: Longman) p 719
[78] Atou T, Kawai N, Ito S, Yubuta K and Kikuchi M 2010 *J. Appl. Phys.* **108** 093523
[79] Atou T, Kawai N, Kondo K, Ito S and Kikuchi M 2010 Proc. 11th HVIS at press
[80] Hongo T, Atou T, Ito S, Yubuta K, Kikuchi M, Nakamura K G, Kusaba K, Fukuoka K and Kondo K 2007 *Phys. Rev.* B **76** 104114
[81] Goto T and Syono Y 1984 *Materials Science of the Earth's Interior* ed I Sunagawa (Tokyo: Terra scientific) p 605
[82] Ahrens T J, Anderson D L and Ringwood A E 1969 *Rev. Geophys.* **7** 667
[83] Stöffler D 1972 *Fortschr. Mineral.* **49** 50
[84] Goltrant O, Leroux H, Doukhan J C and Cordier P 1992 *Phys. Earth Planet. Inter.* **74** 219
[85] Kitamura M, Goto T and Syono Y 1977 *Contrib. Mineral. Petrol.* **61** 299
[86] Kawai N, Atou T, Nakamura K G, Kondo K, Ito S, Yubuta K and Kikuchi M 2009 *J. Appl. Phys.* **106** 023525
[87] Bustingorry S and Jagla E A 2004 *Phys. Rev.* B **69** 064110
[88] Whipple F L 1947 *Astron. J.* **1161** 131
[89] Christiansen E L, Crews J L, Williamsen J E, Robinson J H and Nolen A M 1995 *Int. J. Impact Eng.* **17** 217
[90] Kawai N, Harada Y, Yokoo M, Atou T, Nakamura K G and Kondo K 2008 *Int. J. Impact Eng.* **35** 1612
[91] Harrison W A, Kraut E A, Waldrop J R and Grant R W 1978 *Phys. Rev.* B **18** 4402
[92] Noguera C 2000 *J. Phys.: Condens. Matter* **12** R367
[93] Goniakowski J, Finocchi F and Noguera C 2008 *Rep. Prog. Phys.* **71** 016501
[94] Ohtomo A and Hwang H Y 2004 *Nature* **427** 423
[95] Roessler D M and Walker W C 1967 *Phys. Rev.* **159** 733
[96] Schintke S, Messerli S, Pivetta M, Patthey F, Libioulle L, Stengel M, De Vita A and Schneider W-D 2001 *Phys. Rev. Lett.* **87** 276801
[97] Tsukada M and Hoshino T 1982 *J. Phys. Soc. Japan* **51** 2562
[98] Goniakowski J, Noguera C and Giordano L 2004 *Phys. Rev. Lett.* **93** 215702
[99] Arita R, Tanida Y, Entani S, Kiguchi M, Saiki K and Aoki H 2004 *Phys. Rev.* B **69** 235423
[100] Goniakowski J, Noguera C and Giordano L 2007 *Phys. Rev. Lett.* **98** 205701
[101] Chen Y, Ko H-J, Hong S-K and Yao T 2000 *Appl. Phys. Lett.* **76** 559
[102] Chen Y, Hong S-K, Ko H-J, Kirshner V, Wenisch H, Yao T, Inaba K and Segawa Y 2001 *Appl. Phys. Lett.* **78** 3352
[103] Craft H S, Ihlefeld J F, Losego M D, Collazo R, Sitar Z and Maria J-P 2006 *Appl. Phys. Lett.* **88** 212906
[104] Goodrich T L, Parisi J, Cai Z and Ziemer K S 2007 *Appl. Phys. Lett.* **90** 042910
[105] Kiguchi M, Entani S, Saiki K, Goto T and Koma A 2003 *Phys. Rev.* B **68** 115402
[106] Susaki T, Kumada S, Katase T, Matsuzaki K, Miyakawa M and Hosono H 2009 *Appl. Phys. Express* **2** 091403
[107] Matsuzaki K, Hosono H and Susaki T 2010 *Phys. Rev.* B **82** 033408
[108] Yoshimoto M, Maeda T, Ohnishi T, Koinuma H, Ishiyama O, Shinohara M, Kubo M, Miura R and Miyamoto A 1995 *Appl. Phys. Lett.* **67** 2615
[109] Ohta H, Hirano M, Nakahara K, Maruta H, Tanabe T, Kamiya M, Kamiya T and Hosono H 2003 *Appl. Phys. Lett.* **83** 1029
[110] Kamiya T, Ohta H, Kamiya M, Nomura K, Ueda K, Hirano M and Hosono H 2004 *J. Mater. Res.* **19** 913
[111] Posadas A, Walker F J, Ahn C H, Goodrich T L, Cai Z and Ziemer K S 2008 *Appl. Phys. Lett.* **92** 233511
[112] Ventrice C A Jr, Bertrams Th, Hannemann H, Brodde A and Neddermeyer H 1994 *Phys. Rev.* B **49** 5773
[113] Barbier A, Mocuta C, Kuhlenbeck H, Peters K F, Richter B and Renaud G 2000 *Phys. Rev. Lett.* **84** 2897
[114] Barbier A, Mocuta C and Renaud G 2000 *Phys. Rev.* B **62** 16056
[115] Lazarov V K, Plass R, Poon H C, Saldin D K, Weinert M, Chambers S A and Gajdardziska-Josifovska M 2005 *Phys. Rev.* B **71** 115434